



**HAL**  
open science

## Synergy of nanoconfinement and promotion in the design of efficient supported iron catalysts for direct olefin synthesis from syngas

Bang Gu, Shun He, Deizi Peron, Debora Strossi Pedrolo, Simona Moldovan, Mauro Ribeiro, Bruno Lobato, Petr Chernavskii, Vitaly Ordonsky, Andrei Khodakov

### ► To cite this version:

Bang Gu, Shun He, Deizi Peron, Debora Strossi Pedrolo, Simona Moldovan, et al.. Synergy of nanoconfinement and promotion in the design of efficient supported iron catalysts for direct olefin synthesis from syngas. *Chinese Journal of Catalysis*, 2019, 376, pp.1-16. 10.1016/j.jcat.2019.06.035 . hal-02185085

**HAL Id: hal-02185085**

**<https://hal.science/hal-02185085>**

Submitted on 25 Oct 2021

**HAL** is a multi-disciplinary open access archive for the deposit and dissemination of scientific research documents, whether they are published or not. The documents may come from teaching and research institutions in France or abroad, or from public or private research centers.

L'archive ouverte pluridisciplinaire **HAL**, est destinée au dépôt et à la diffusion de documents scientifiques de niveau recherche, publiés ou non, émanant des établissements d'enseignement et de recherche français ou étrangers, des laboratoires publics ou privés.



Distributed under a Creative Commons Attribution - NonCommercial 4.0 International License

Revision, June 16<sup>th</sup>, 2019

# **Synergy of Nanoconfinement and Promotion in the Design of Efficient Supported Iron Catalysts for Direct Olefin Synthesis from Syngas**

*Bang Gu<sup>a</sup>, Shun He<sup>b</sup>, Deizi V. Peron<sup>a</sup>, Debora R. Strossi Pedrolo<sup>a</sup>, Simona Moldovan<sup>c</sup>, Mauro C. Ribeiro<sup>d</sup>, Bruno Lobato<sup>e</sup>, Petr A. Chernavskii<sup>f</sup>, Vitaly V. Ordonsky<sup>a\*</sup> and Andrei Y. Khodakov<sup>a\*</sup>*

<sup>a</sup>*Univ. Lille, CNRS, Centrale Lille, ENSCL, Univ. Artois, UMR 8181 – UCCS – Unité de Catalyse et Chimie du Solide, F-59000 Lille, France.*

<sup>b</sup>*Collaborative Innovation Center of Chemistry for Energy Materials, State Key Laboratory of Physical Chemistry of Solid Surfaces, Xiamen University, 361000 Xiamen, China.*

<sup>c</sup>*Groupe de Physique des Matériaux, CNRS, Université Normandie & INSA Rouen Avenue de l'Université - BP12, 76801 St Etienne du Rouvray.*

<sup>d</sup>*Instituto de Ciências Exatas, Universidade Federal Fluminense, Volta Redonda, RJ, Brazil.*

<sup>e</sup>*Federal Rural University of Rio de Janeiro, Chemical Engineering Department, BR-465, Km 7, Seropédica, CEP 23897-000, Brazil.*

<sup>f</sup>*Department of Chemistry, Moscow State University, 119992 Moscow, Russia.*

Corresponding authors:

vitaly.ordonsky@univ-lille.fr and andrei.khodakov@univ-lille.fr

## Abstract

Light olefins are important building blocks in chemical industry. High temperature Fischer-Tropsch synthesis provides a remarkable opportunity for direct synthesis of light olefins from syngas derived from a wide range of alternative feedstocks (biomass, organic or plastic wastes, natural gas, shale gas or coal). The present work focuses on the combined effects of the iron nanoconfinement, on the one hand, and promotion with bismuth and lead, on the other hand, on the structure and catalytic performance of iron catalysts supported by carbon nanotubes in high temperature Fischer-Tropsch synthesis. A wide range of techniques (TEM, XRD, TPR, synchrotron-based XPS, *in-situ* XANES and *in-situ* magnetic measurements) was used to characterize the catalysts. Iron carbidization proceeds much easier for iron species confined inside carbon nanotubes and promoted with Bi and Pb. Iron nanoconfinement inside carbon nanotubes combined with the promotion with Bi or Pb result in a 10-fold higher yield of light olefins. Nanoconfinement in carbon nanotubes mostly leads to better iron dispersion and stability, while the intrinsic activity is only slightly affected. Promotion with Bi and Pb results in a major increase in the site intrinsic activity in both confined and non-confined catalysts. Moreover, over the optimised promoted and confined catalysts, Fischer-Tropsch synthesis occurs even under atmospheric pressure with high conversion and enhanced selectivity to light olefins.

**Keywords:** Fischer-Tropsch; *in-situ* XANES; light olefins; nanoconfinement; promotion; catalyst stability

## 1. Introduction

Light olefins ( $C_2-C_4$ ) are key building blocks in the chemical industry [1–3]. Nowadays, light olefins are produced from thermal cracking of naphtha, ethane cracking or methanol-to-olefins (MTO) process. High temperature Fischer-Tropsch (FT) synthesis is an attractive alternative for direct transformation of renewable and alternative carbon feedstocks into lower olefins via intermediate formation of syngas. The selectivity to lower olefins in FT synthesis over iron-based catalysts remains a major challenge, because of unselective broad Anderson-Schulz-Flory (ASF) distribution of the produced hydrocarbons [2]. In the conventional FT synthesis, the maximum selectivity to the  $C_2-C_4$  hydrocarbons (including both olefins and paraffins) is around 58% with the chain growth probability ( $\alpha$ ) of 0.46. Higher yield of olefins in high temperature FT synthesis can be obtained by optimization of the structure of iron catalysts and their catalytic performance. Recently, Bao's [4] and Wang's [5] groups proposed new strategies for conversion of syngas to olefin. These strategies combine conversion of syngas to methanol (or ketene) with subsequent conversion of the oxygenated intermediates to light olefins. High olefin selectivities have been reported, though the catalyst stability for this multistep reaction could be still a challenge.

Optimization of the catalytic performance of iron catalysts in FT synthesis can be addressed by catalyst promotion [6]. Most commonly, the promoters of iron FT catalysts are divided in two classes. The structural promoters affect the formation and stability of the catalysts and its active phase, while the electronic promoters modify the local electronic structure of active metals mostly by adding or withdrawing

electron density. The electronic promoters also directly affect adsorption/desorption and elementary reaction steps. Alkali ions are most common promoters of iron FT catalysts. They have a noticeable effect on both the activity and selectivity of iron catalysts [7]. Other promoters and/or supports (e.g. CuO, Al<sub>2</sub>O<sub>3</sub> and SiO<sub>2</sub>) mainly facilitate iron reduction, stabilize a high metal surface area or improve the catalyst mechanical properties. Combined promotion of iron catalysts with sodium and sulphur was shown [1,8] to improve the selectivity to light olefins. Higher olefin selectivity was observed over those catalysts at low conversions and coincided the decrease in the overall catalytic activity. Recently our group has found [9,10] extremely strong promoting effects of soldering metals such as Bi and Pb on the catalytic performance of supported iron catalysts. The promoting effects of Bi and Pb on iron catalysts have been reinforced by their migration during the catalyst activation and their preferential localization at the surface of iron carbide nanoparticles leading to the core-shell structures. The soldering promoters (Bi and Pb) enhance the CO dissociation by scavenging an oxygen atom with formation of CO<sub>2</sub> [9,10].

In addition to the promotion, nanoconfinement of active phase into porous matrices has been also an efficient way to improve the activity and selectivity of the Fe [11–14], Co [15], Ni [16], Ru [17] and Rh [18] catalysts for CO hydrogenation. The nanoconfinement may potentially bring different benefits for the catalytic performance of iron catalysts such as better reducibility and carbidization, higher metal dispersion, electronic effects, better stability and shape selectivity effect on the intermediates and reaction products.

The nanoconfinement of iron nanoparticles can be achieved in mesoporous oxides, mesoporous zeolites and porous carbon materials. Metal nanoparticle nanoconfinement within carbon nanotubes (CNT) [19] has been particularly remarkable. Bao [20–24] et al found that iron species located inside the CNT tubes had better reducibility and facilitated formation of active iron carbide phase compared to iron located outside the CNT channels. The resulting catalysts showed enhanced activity in low temperature FT synthesis and favoured formation of the C<sub>5+</sub> hydrocarbons. The same group investigated [22,23] the catalytic performance of the CNT confined Fe and FeN catalysts in direct olefin synthesis from syngas. Recently we found [25] that the size of iron nanoparticles located inside CNT has a strong effect on the intrinsic activity. The increase in the sizes of iron nanoparticle confined inside CNT from 2.5 to 12 nm resulted in a gradual increase in the intrinsic catalyst activity. The obtained hydrocarbon distributions were, however, similar over the confined and non-confined catalysts with the selectivity to lower olefins of around 30–40%.

Our present work focuses on the synergetic effects arising from the combination of the nanoconfinement of iron nanoparticles in CNT and their promotion with Bi and Pb on the structure, catalytic performance and stability of iron catalysts in high temperature FT synthesis. A combination of nanoconfinement and promotion results in the extremely high catalytic activity of iron catalysts even at atmospheric pressure with enhanced selectivity to light olefins. In order to shed some light onto the understanding of this effect, a thorough characterization of these catalysts was

attempted via XRD, XPS, *in-situ* XANES, TEM-EDX, H<sub>2</sub>-TPR, CO-TPR, *in-situ* magnetization measurements, ICP and BET. The characterization data are discussed alongside with the catalytic results in high temperature FT synthesis obtained in a fixed bed reactor under a wide range of operating conditions.

## 2. Experimental

### 2.1 CNT treatments

The treatments of CNTs (Iolitec nanomaterial, 95%, inner diameter 5-12 nm, outer diameter 10-30 nm) were performed according to previous literature [18]. Prior to the impregnation, CNTs were treated with nitric acid in order to open the tube channels, to remove contaminations with metals and to make the CNT hydrophilic. Opening of CNT was ensured by treating CNT (3.0 g) in concentrated HNO<sub>3</sub> (68%, 210 mL) for 14 h at 140 °C under reflux. The treated samples were then filtered, washed with distilled water and dried in the oven. The CNTs with closed tubes were obtained by their treatment with nitric acid under milder conditions (34 wt. % HNO<sub>3</sub> for 6h at 110 °C).

### 2.2 Catalyst preparation

The iron catalysts were prepared by incipient wetness impregnation of the CNT support with aqueous solutions of iron nitrate (Fe(NO<sub>3</sub>)<sub>3</sub>·9H<sub>2</sub>O, Sigma-Aldrich). Lead nitrate (Pb(NO<sub>3</sub>)<sub>2</sub>, Sigma-Aldrich) and bismuth nitrate (Bi(NO<sub>3</sub>)<sub>3</sub>·5H<sub>2</sub>O, Sigma-Aldrich) were used for preparation of the Bi- and Pb-promoted iron catalysts

by co-impregnation. The catalysts containing iron species on the outer surface were prepared using CNT with closed tubes, while the CNT with open tubes were used for preparation of iron catalysts containing iron species inside the CNT. The aqueous solution was drawn into the CNT channels by capillary forces aided by ultrasonic treatment and stirring following the procedure from the literature [20,24]. The Fe loading was fixed at 10 wt. %. The molar ratios of Fe/Pb and Fe/Bi were 100/2. After the impregnation, the samples were dried in an oven at 80 °C for 12 h followed by thermal treatment (calcination) at 400 °C for 4 h under a flow of nitrogen (50 mL/min). The calcined catalysts are labeled as FeM/CNT-in or FeM/CNT-out, where “M” stands for the promoters (Bi or Pb), “in” represents iron inside the CNT tubes and “out” represents iron outside the CNT tubes.

### *2.3. Catalyst characterization*

Low temperature N<sub>2</sub> adsorption-desorption experiments were performed on a Micromeritics Tristar Model 3020 Surface Area and Porosimetry analyzer. 0.1g of the sample was degassed under vacuum at 250 °C for 2 h, then N<sub>2</sub> was used as adsorbate. The nitrogen isotherms were measured at -196°C. The specific surface area of the sample was calculated by the BET method from the isotherms between P/P<sub>0</sub>=0.05 and 0.3.

The X-ray diffraction patterns (XRD) were recorded on a PANalytical Empyrean X-ray diffractometer in Bragg-Brentano configuration with the 0.02° step size and 1 s step time. The Cu K $\alpha$  radiation (40 kV and 30 mA) was used as the X-ray source. The

crystalline phases were identified by comparing the diffraction patterns with those of the standard powder XRD files (JCPDS). The crystallite average size was calculated using the Scherrer equation. H<sub>2</sub>-TPR and CO-TPR measurements were performed on Micrometrics AutoChemII 2920 instrument.

*Ex-situ* and *in-situ* Fe K-edge and Bi L<sub>3</sub>-edge X-ray absorption fine structure (XAFS) spectra were measured at Beamline XDS, Laboratório Nacional de Luz Síncrotron (LNLS, Campinas, Brazil) with electron beam energy of 5-30 KeV. The data were collected in the transmission mode, Si (111) and Si (311) monochromators. The data were analyzed with the Athena software.

The synchrotron XPS was also measured in LNLS at the SXS beamline. The spectra were collected using an InSb (111) double crystal monochromator at the fixed photon energy of 1840 eV. The hemispherical electron analyzer (Physical Electronics model 10-360) was set at a pass energy of 23.5 eV, and the energy step was 0.1 eV, with an acquisition time of 500 ms per point. The C 1s peak value of 284.5 eV is used as a reference to verify possible charging effects. The samples were placed on onto silicon wafers thoroughly cleaned with the “piranha” solution and placed into the *in-situ* reaction cell with the treatment of CO or syngas (H<sub>2</sub>/CO=1/1, p=1 atm) at 350 °C for 90 min. The treated samples were then transferred under vacuum to the analytical chamber to record the XPS spectra.

Quantitative elemental analyses of the catalysts were performed by inductively coupled plasma-optic emission spectroscopy 720-ES ICP-OES (Agilent) with axially viewing and simultaneous CCD detection. The quantitative determination of metal

content in the catalysts was made based on the calibration with the certificated standard solutions. The ICP Expert<sup>TM</sup> software (version 2.0.4) provided the metal concentrations in the samples allowing estimation of the weight percentage of components. The H<sub>2</sub> temperature-programmed reduction (H<sub>2</sub>-TPR) and CO-temperature programmed reduction (CO-TPR) experiments were carried out using the AutoChem II 2920 apparatus (Micromeritics) using 0.05 g of the sample in a flow of H<sub>2</sub>/Ar (5 vol. % H<sub>2</sub>) or CO/Ar (5 vol. % CO) stream (30 ml/min). The temperature was increased from room temperature to 900 °C at the rate of 10 °C/min.

The TEM (Transmission Electron Microscopy) analyses were carried out on a double corrected Cold FEG ARM Jeol 200 (field emission gun) microscope operated at 200 kV. High quality analytical explorations were carried out using the 100 mm Centurio detector for the energy dispersive X rays (EDX) equipping this TEM. The point-to-point resolution reached was of the order of 78 pm under the parallel TEM mode and 0.9 Å under the STEM (Scanning TEM) mode. Z-sensitive high angle annular dark field, HAADF–scanning transmission electron microscopy (STEM) imaging, and EDX elemental maps were performed using scanning speed 20 μs/px for imaging and 0.05 μs/px for EDX (256x256px maps), with a 0.1 nm probe size and a current of 120pA. More than 30 areas and 250 particles were explored to estimate the average Fe particle size and standard deviation from the TEM images.

The magnetic characterization was performed using a Föner vibrating-sample magnetometer equipped with an *in-situ* cell [26,27]. The magnetometer was calibrated using 1 mg of pure metallic Fe before each experiment. Typically, 0.01g of the

sample was heated to 350 °C with a 4.7 °C/min ramping rate under the CO flow (15 ml min<sup>-1</sup>) for 120 min. After the activation, the sample was cooled to the room temperature in the flow of CO. During the whole treatment, the saturation magnetization curve was recorded *in-situ* by the magnetometer. The pretreatment with syngas was performed using the same procedure.

#### 2.4. Catalytic tests

The syngas conversion was performed in a fixed-bed reactor (8 mm inner diameter). 0.1 g of the fresh catalyst was loaded into the stainless steel tube. The catalysts were activated by heating up to 350 °C at a rate of 5 °C min<sup>-1</sup> and dwelling at 350 °C for 10 h under CO flow (50 ml min<sup>-1</sup>) at atmosphere pressure. After cooling down to 180 °C, syngas with H<sub>2</sub>/CO = 1/1 was introduced into the reactor. The mass flow meter was used to control the flow rate. The required reaction pressure is achieved by a back-pressure valve. Nitrogen with a flow of 1 ml min<sup>-1</sup> in the syngas was used as an internal standard for the calculation of CO conversion. After the pressure and flow rate have been stabilized, the temperature is raised (1 °C min<sup>-1</sup>) to 350 °C to start the reaction.

The reagents and reaction products were analyzed by a gas chromatograph (Bruker GC-450), which was equipped with a thermal conductivity detector (TCD) and a flame ionization detector (FID). A packed CTR-1 column was connected to the TCD, and a Rt-Q-PLOT capillary column was connected to the FID. The liquid products (oil, wax and water phases) were collected in a cold trap kept at 20 °C and analyzed

off-line by gas chromatography. Iron time yields (FTY) were expressed as moles of CO converted per gram of total iron per second. Apparent turnover frequency (TOF) was calculated [28,29] using the bulk density of  $\text{Fe}_5\text{C}_2$  ( $\rho = 7.57 \text{ g mL}^{-1}$ ) and assuming the surface density of 14 Fe atoms  $\text{nm}^{-2}$ . Similar to the report of de Jong's group [29], TOF was calculated relative to the  $\text{Fe}_5\text{C}_2$  site. The  $\text{CO}_2$  free hydrocarbon selectivities calculated on carbon basis were calculated taking into account only hydrocarbon production in FT synthesis. The carbon balance was better than 90%. The details of conversion and selectivity calculations are given in **Supplementary Material (SM)**.

### **3. Results and discussion**

#### *3.1 Catalyst characterization*

##### *3.1.1 Structure and morphology*

The ICP elemental analysis and nitrogen adsorption data are displayed in **Table 1**. Both catalysts with non- confined and confined iron nanoparticles had similar iron content (around 10 wt.%), while the Bi and Pb contents were close to 0.8 wt. % in the promoted catalysts. The ICP results are therefore similar to the catalyst inventory composition. **Table 1** also shows textural properties of the CNTs support and iron catalysts containing iron nanoparticles located either outside or inside the CNTs tubes. As expected, the CNTs with closed tubes exhibit lower surface area compared with CNTs with open tubes. The impregnation of CNTs with iron and promoters decreases both the surface area and pore volume (**Table 1**). Interestingly, iron impregnation

produces only a very small impact on the pore volume of CNT with closed tubes (from 0.54 cm<sup>3</sup>/g to 0.52 cm<sup>3</sup>/g). However, when the iron is located inside the CNTs tubes, the pore volume decreases very significantly (from 0.83 cm<sup>3</sup>/g to 0.50 cm<sup>3</sup>/g). This is consistent with the iron nanoparticle localization inside the CNT tubes and partial blocking of the pore volume by iron species introduced via impregnation.

**Figure 1a** displays XRD profiles of the supported iron catalysts. The diffraction lines at 26.3° and 43.8° are attributed to the (002) and (101) reflections of the CNT supports. The peaks at 2θ of 35.6° are assignable to the hematite phase (Fe<sub>2</sub>O<sub>3</sub>, JCPDS 13-0534), while the peaks at 2θ of 35.8°, 43.5° and 53.9° can be attributed to the magnetite phase (Fe<sub>3</sub>O<sub>4</sub>, JCPDS 75-0449). It is clear that the width of iron oxide XRD peaks for the catalysts containing iron nanoparticles outside the CNT tubes is smaller than for their counterparts with confined iron nanoparticles. This is indicative of the larger size of iron oxide nanoparticles located outside the CNT with the same iron content. These results are consistent with previous reports [20,30]. Indeed, iron nanoconfinement inside CNT reduces the size of iron oxide nanoparticles possibly because of steric constraints for the iron nanoparticle growth. The XRD results also suggest that the Bi or Pb promotion does not noticeably affect the iron oxide phase composition and dispersion in the catalysts containing iron oxide nanoparticles located outside CNT or confined within CNT.

X-ray absorption near edge structure (XANES) of the calcined non-confined and CNT confined iron-based catalysts at iron K-absorption edge has provided information about iron coordination and iron oxidation state [31] (**Figure 1b**). Bulk

FeO, Fe<sub>2</sub>O<sub>3</sub>, Fe<sub>3</sub>O<sub>4</sub> and Fe foil have been used as references (**Figure S1, SM**). All iron oxides (except for FeO) show a pre-edge feature at 7113 keV. This pre-edge feature is assigned to the  $1s \rightarrow 3d$  electron transition [32]. The six examined CNT supported iron-based catalysts show almost identical shape of the K-edge (**Figure 1b**). The shape of the K-edge indicates coexistence of Fe<sub>2</sub>O<sub>3</sub> and Fe<sub>3</sub>O<sub>4</sub> in the catalysts pretreated in nitrogen. The fractions of Fe<sub>2</sub>O<sub>3</sub> and Fe<sub>3</sub>O<sub>4</sub> calculated from the XANES interpolation procedure (ATHENA software) using the spectra of reference iron oxides are shown in **Table 2**. A slightly higher concentration of Fe<sub>3</sub>O<sub>4</sub> was observed, when iron nanoparticles are encapsulated inside carbon nanotubes in FeBi/CNT-in.

**Figure 2** displays the TEM micrographs of the fresh non-confined and confined iron CNT supported catalysts. The TEM images for the iron Fe/AC catalyst supported on active carbon are also given for comparison (**Figure S2, SM**). The Fe/AC catalyst presents iron oxide particles with the average size of 12 nm. The TEM images confirm successful introduction of iron nanoparticles inside the CNTs tubes. Indeed, about 80% of iron particles are located within the inner channels of the CNTs. This can be attributed to the tubular morphology of CNTs, which can induce capillary forces by actually sipping the Fe nitrate containing solution inside the tubes during the impregnation process [33]. The iron oxide particles located outside CNT tubes in Fe/CNT-out, FeBi/CNT-out, FePb/CNT-out exhibit a broad particle size distribution of 4-14 nm with the average size of 9 nm (**Table 1, Figure S3, SM**). On the contrary, the size distributions of iron oxide nanoparticles located inside the CNTs tubes in the Fe/CNT-in, FeBi/CNT-in and FePb/CNT-in catalysts are very narrow with the

average particles size of ~ 5 nm (**Figure S3, SM**). Importantly, iron nanoconfinement inside CNT leads to the decrease in the iron oxide particle size. Smaller iron particle size inside CNT can be caused by their spatial nanoconfinement in CNTs. This phenomenon has been previously observed for the Fe [34] and Co [35] metals. Moreover, the size of iron oxide nanoparticles is close to the inner diameter of CNT (5-14 nm). The growth of iron oxide nanoparticles during decomposition of iron nitrate seems to be limited by the inner CNT walls. Furthermore, the Bi and Pb promoters do not affect the iron oxide morphology. The iron oxide particle size distributions are similar in iron monometallic and promoted catalysts. These results are in agreement with the XRD results.

### *3.1.2 Iron reducibility and carbidization*

Good iron reducibility and carbidization are essential for obtaining high activity of iron catalysts in FT synthesis. First, we examined reducibility and carbidization of iron oxide species in the confined and non-confined catalysts by H<sub>2</sub>-TPR and CO-TPR (**Figure 3**). All H<sub>2</sub>-TPR profiles (**Figure 3a**) display three main well-separated reduction peaks, which are attributed to the multi-step iron reduction from Fe<sub>2</sub>O<sub>3</sub> hematite to metallic iron [9]. In agreement with the literature [12,36,37], the first peak at 250-420 °C can be ascribed to the reduction of Fe<sub>2</sub>O<sub>3</sub> to Fe<sub>3</sub>O<sub>4</sub>, the second peak can be assigned to the reduction of Fe<sub>3</sub>O<sub>4</sub> to FeO, whereas the third peak at 600-700°C can be attributed to the reduction of FeO to metallic Fe. **Figure 3a** shows that each reduction step occurs at lower temperatures in confined Fe/CNT-in in

comparison with non-confined Fe/CNT-out. This suggests that nanoconfinement facilitates iron reduction. Interestingly, the promotion with Bi and Pb does not affect the positions of TPR peaks in the non-confined catalysts. The only difference is some increase in the total H<sub>2</sub> consumption (**Table 1**) over the promoted non-confined catalysts relative to the unpromoted Fe/CNT-out counterpart. In the confined Fe/CNT-in catalysts however, the promotion with Bi and Pb results in the 30 °C shift of the reduction peaks to lower temperatures. Some increase in the H<sub>2</sub> consumption was also observed in FeBi/CNT-in and FePb/CNT-in (**Table 1**).

The CO-TPR profiles are shown in **Figure 3b**. All the catalysts exhibit two broad peaks. Previously it was shown [38–42] that carbidization of hematite proceeds via intermediate formation of magnetite according to the schema: Fe<sub>2</sub>O<sub>3</sub>→Fe<sub>3</sub>O<sub>4</sub>→Fe<sub>x</sub>C. Similar to the H<sub>2</sub>-TPR profiles, the CO-TPR peaks of the confined Fe/CNT-in catalysts shift to lower temperatures relative to the non-confined Fe/CNT-out counterparts. The effect of the promotion with Bi and Pb on the CO-TPR profiles can be only seen for the confined iron catalysts. The peaks in CO-TPR for the FeBi/CNT-in and FePb/CNT-in shift to lower temperatures compared to the unpromoted Fe/CNT-in. Thus, the confined iron nanoparticles exhibit higher reducibility and carbidization than the non-confined counterparts. In addition, the Bi and Pb promoters in the catalysts containing iron nanoparticles inside the CNT tubes decrease activation energy. The reduction/carbidization processes occur at significantly lower temperatures and the extents of iron reduction or carbidization are improved.

Several Fe phases, including  $\alpha$ -Fe, Fe<sub>3</sub>O<sub>4</sub>, Fe<sub>3</sub>C, Fe<sub>2.2</sub>C, Fe<sub>5</sub>C<sub>2</sub> and Fe<sub>7</sub>C<sub>3</sub> have been reported [42] in freshly activated or used iron-based FT catalysts. Iron carbides are commonly considered to be active phase [43,44] in FT synthesis. The evolution of Fe catalysts during activation or FT reaction and identity of the active phase remain controversial. STEM-HAADF and STEM-EDS analyses have been performed to elucidate the localization of iron and promoters and morphology evolution during the activation and reaction (**Figures 4, 5 and 6**). In the STEM-HAADF images, the image intensity correlates with the Z-atomic number of the constitutive elements, such that the Bi species correspond to brighter compared with the iron-rich areas within the nanoparticles. **Figure 4** shows in the fresh FeBi/CNT-in catalysts, the iron and Bi are located inside the CNT tubes and Bi particles are uniformly mixed with Fe nanoparticles. The iron particles present pod-like morphology with the average particle size of ~ 5 nm. Interestingly, the core-shell structure was formed with the average particle size of ~ 8 nm during activation in CO, most of the Bi particles are present in the shell structure (**Figure 5**). The iron and bismuth distributions and morphology evolves after activation in CO. When Bi species are located outside the CNT tubes, the Bi migrates forming bismuth species on the shell of iron carbide nanoparticles, while some Bi particles remain isolated (**Figure S4, SM**). Similar promoter localization and iron morphology were also observed in the used FeBi/CNT-in catalysts (**Figure 6**). Some iron particles also migrate to outer surface of CNT and undergo significant sintering yielding iron particles of ~15 nm diameter. In addition, there are still many iron particles situated inside the CNT channels.

Interestingly, the size of the iron nanoparticles located inside CNT remain unchanged after the activation in CO.

The XRD profiles of the catalysts activated under CO at 350 °C and after reaction are displayed in **Figure S5, SM**. Both the activated and used catalysts show a broad peak at ca. 44°, which can be assigned to iron carbides ( $\chi$ -Fe<sub>5</sub>C<sub>2</sub>,  $\epsilon$ -Fe<sub>2.2</sub>C). Due to significant broadening and overlapping of the iron carbide XRD peaks, the unambiguous identification of the specific  $\chi$ -Fe<sub>5</sub>C<sub>2</sub> or  $\epsilon$ -Fe<sub>2.2</sub>C carbide phases and measuring the iron carbide crystallites sizes from XRD peak broadening seem rather challenging from XRD patterns.

The subsurface structure of CNT supported iron-based catalysts was characterized by XPS (**Figure 7**). The Fe 2p peaks of fresh Fe/CNT-out, FeBi/CNT-out and FeBi/CNT-in appear at ~711.2 eV (Fe2p<sub>3/2</sub>) and ~724.6 eV (Fe 2p<sub>1/2</sub>) with a shakeup satellite peak at ~719.2 eV. After catalyst treatment with CO at 350 °C for 90 min, the intensity of XPS peak for Fe<sup>3+</sup> decreases. A broad shoulder with the binding energy of 707.3 eV assignable to iron carbide [45] was detected. After exposure to syngas (H<sub>2</sub>/CO = 1/1) for 90 min, higher amount of iron carbide has been formed due to further carbonization. Interestingly, the intensity of iron carbide peak at binding energy at ~707.3 eV is higher in the Bi promoted and CNT confined FeBi/CNT-in catalyst activated in CO and syngas compared to the FeBi/CNT-out and Fe/CNT-out counterparts (**Figure 7**). These results are consistent with higher extent of iron carbidization in the confined and promoted catalysts. During XPS experiments, iron carbidization was performed in the reactor chamber of the synchrotron XPS

spectrometer. Because of shorter carbidization time and chamber geometry, the extent of iron carbidization could be somewhat lower compared to the experiments conducted in the catalytic reactor.

### 3.1.3. *In-situ investigation of iron carbidization*

Further information about the type and concentration of iron carbides in non-confined and confined catalysts was obtained from *in-situ* XANES and *in-situ* magnetic measurements. The XANES experiments were performed with an *in-situ* spectroscopic cell under realistic activation conditions. **Figure 8** displays evolution of the Fe K-edge XANES spectra as the temperature increases from 30 to 350 °C under CO or syngas. The fractions of iron oxides and iron carbides present *in-situ* during the catalyst activation were evaluated using the XANES decomposition with the spectra of reference compounds (**Figure 9**). Iron-based catalysts undergo phase change from Fe<sub>2</sub>O<sub>3</sub> to Fe<sub>3</sub>O<sub>4</sub> and then to Fe<sub>x</sub>C<sub>y</sub> during the carbidization [38–42]. For the non-confined Fe/CNT-out catalyst (**Figure 8a**), the reduction of Fe<sub>2</sub>O<sub>3</sub> to Fe<sub>3</sub>O<sub>4</sub> is quite easy (> 120 °C), however, the conversion of Fe<sub>3</sub>O<sub>4</sub> to Fe<sub>x</sub>C<sub>y</sub> is a much slower process even at 350 °C. After subsequent exposure to syngas at 350 °C, the iron phase composition does not change a lot compared to that obtained in the presence of CO. The catalysts still contain a mixture of Fe<sub>3</sub>O<sub>4</sub> and Fe<sub>x</sub>C<sub>y</sub> (**Figure 8b**). **Figures 8c** and **d** show the iron phase transformation in FeBi/CNT-out catalyst during exposure to CO. The carbidization of Fe<sub>3</sub>O<sub>4</sub> to Fe<sub>x</sub>C<sub>y</sub> is facilitated in the presence of Bi. The carbidization proceeds much better over FeBi/CNT-out relative to Fe/CNT-out. After

the contact of FeBi/CNT-out with syngas for 1 h at 350 °C, the XANES spectra do not evolve anymore. This suggests that no additional iron carbide phase forms in syngas during the FT reaction. Interestingly, when iron nanoparticles are located inside the CNT channels, this Bi promotion effect is much stronger. The iron carbidization occurs at temperature 44 °C lower over confined FeBi/CNT-in compared with the non-confined FeBi/CNT-out catalyst (**Figure 8e**). The iron phase composition after carbidization at 350°C is shown in **Table 2**. An enhancement of carbidization in the presence of the Bi promoter and under nanoconfinement is clearly observed.

Less information is usually available about the promoters compared to the active iron phases. This is often due to lower promoter concentration in the catalysts that precludes the effectiveness of standard characterization techniques, such as XRD and TEM. Here, *in-situ* XANES spectra at the L<sub>3</sub>-edge of Bi are also applied to follow the evolution of Bi phases during CO activation and reaction (**Figure 10**). The fractions of bismuth oxide and metallic bismuth were calculated from decomposition of XANES using spectra of reference Bi<sub>2</sub>O<sub>3</sub> and metallic bismuth (**Figure 9**). XANES is indicative of the presence of the Bi<sub>2</sub>O<sub>3</sub> phase in the fresh catalysts. The Bi<sub>2</sub>O<sub>3</sub> oxide is gradually reduced to metallic Bi during CO treatment from 50 °C to 350 °C. Interestingly, the confined FeBi/CNT-in catalyst show easier reducibility of Bi oxides during activation in CO relative to non-confined FeBi/CNT-out. The metallic Bi phase forms at ~ 50 °C lower temperature in FeBi/CNT-in compared with non-confined FeBi/CNT-out. After 90 min of activation in CO, syngas (H<sub>2</sub>/CO=1/1) was introduced the catalysts. Importantly, Bi remains mostly in the metallic form

during the reaction in the presence of syngas at the temperatures from 180 °C to 350 °C.

Thus, the *in-situ* XANES results reveal that in both the non-confined and confined iron-based catalysts in the presence of CO, Fe<sub>2</sub>O<sub>3</sub> is first reduced to Fe<sub>3</sub>O<sub>4</sub> and then carburized to Fe<sub>x</sub>C<sub>y</sub>. This process is enhanced in the confined catalysts and in the presence of promoters (Bi and Pb). However, for all three studied catalysts, no noticeable iron phase composition changes occurs during subsequent contact with syngas. This indicates that iron reduction and carburization mainly occur during the activation with CO. The Bi promoter is also reduced during the CO activation and remains mostly metallic in syngas atmosphere. Note that because of accuracy limits of XANES, we cannot rule out the presence of small fraction of bismuth oxide. The Bi reducibility is enhanced in the confined FeBi/CNT-in catalyst.

Furthermore, the *in-situ* magnetic measurements provided further information about the genesis of iron carbides in the confined and non-confined iron catalysts. These measurements were performed at different temperatures under the flow of CO or syngas. Several ferri- or ferromagnetic phases (iron carbides, metallic iron and magnetite) may be present in the treated catalysts. These phases can be identified from their Curie temperatures, which can be evaluated from the dependence of magnetization on the temperatures (thermomagnetic curves). The Curie temperature of  $\chi$ -Fe<sub>5</sub>C<sub>2</sub> is close to 250 °C, while the Curie temperature of magnetite (Fe<sub>3</sub>O<sub>4</sub>) and metallic Fe are 580 °C and 770 °C, respectively [9,46]

**Figure 11** shows the variation of catalyst magnetization with temperature during

cooling the non-confined or confined, unpromoted or promoted iron catalysts after the carbidization in CO or syngas. All the catalysts show similar shape with the Curie temperature of around 250 °C. This suggests that  $\chi$ -Fe<sub>5</sub>C<sub>2</sub> is the predominant iron phase in the carbidized catalysts. Interestingly, both nanoconfinement and promotion affect the extent of iron carbidization. After the *in-situ* CO activation, the non-confined and non-promoted Fe/CNT-out catalyst shows lowest iron carbide concentration, while the Bi and Pb promotions increase the iron carbide concentration even in the non-confined catalysts (**Figure 11a**). Iron nanoconfinement inside CNT increases extent of iron carbidization. Moreover, the confined Fe/CNT-in shows iron carbide concentration comparable with the Bi and Pb promoted but non-confined FeBe/CNT-out and FePb/CNT-out catalysts. The extent of iron carbidization can be further increased after introducing Bi and Pb into the Fe/CNT-in confined catalyst. The iron carbide concentration seems to be slightly higher after activation in syngas compared to the activation in CO (**Figure 11b**).

### 3.2 Catalytic performance

#### 3.2.1. Effect of nanoconfinement and promotion of syngas conversion

The catalytic data in high temperature FT synthesis for the confined and non-confined iron-based catalysts under high pressure (10 bar) are shown in **Tables 3, 4** and **Figures 14, S6, S7, SM**. When the iron particles are located outside the CNT tubes in Fe/CNT-out, the CO conversion observed at the reaction pressure of 10 bar (**Table 3**) is low (14.4%) with the FTY of  $1.6 \times 10^{-4} \text{ mol}_{\text{CO}}\text{g}_{\text{Fe}}^{-1}\text{s}^{-1}$  and high selectivity

to methane (34.2%) is observed. After introducing the Bi and Pb promoters, the CO conversion over FeBi/CNT-out and FePb/CNT-out increases to 28.9% and 34.3%, respectively. The selectivity to methane decreases, however, the selectivity of lower olefins slightly increases and reaches 36%. Interestingly, when the iron particles are located inside the CNT tubes in Fe/CNT-in, the CO conversion and FTY increase from 14.4 to 24.8 % and from 1.6 to 2.8 mol<sub>CO</sub>g<sub>Fe</sub><sup>-1</sup> respectively. These results are consistent with previous works of Bao's group [20–24] et al showing higher activity of the catalysts containing iron nanoparticles inside CNT. Calculation assuming complete carbidization is indicative however, of similar TOF values, when iron nanoparticles are located inside or outside CNT (**Table 3**). This suggests that the enhancement of catalytic activity in the confined catalysts is principally due to higher iron dispersion.

The promotion of the confined Fe/CNT-in catalyst with Bi and Pb results in further important increase in the reaction rate. The CO conversion increases from 24.8 to 60-70% over the Bi and Pb-promoted Fe/CNT-in samples and FTY increases 2.5-3 times from 2.8 to 6.9 and 8.2 mol<sub>CO</sub>g<sub>Fe</sub><sup>-1</sup> s<sup>-1</sup>. The iron time yield reaches 23.4\*10<sup>-4</sup> mol<sub>CO</sub>g<sub>Fe</sub><sup>-1</sup>s<sup>-1</sup> for the FePb/CNT-in catalysts at the total syngas pressure of 20 bar and GHSV of 84 L/g.h which is one of the best results for the iron-based FT synthesis catalysts available so far in the literature (**Table S1, SM**). The TOF values are also higher in the promoted catalysts (**Table 3**). This suggests electronic effects of the promotion with Bi and Pb on the intrinsic activity of iron carbide surface sites. Moreover, the presence of promoters inside the tubes changes the product selectivity

compared with non-confined catalysts. The selectivity to methane decreases from 34% to 25%, while the light olefins selectivity increases from ~33% to ~45%. When a small amount of potassium was added to make the FePbK/CNT-in catalyst, the catalytic performance in FT synthesis was further improved (**Table 3, Figure S6, SM**). The light olefin selectivity reaches 52.6% at the carbon monoxide conversion of 76.2%. The promotion with potassium seems to increase further the light olefin yield over the promoted and confined iron catalysts.

The effects of GHSV and pressure on the CO conversion over the confined and non-confined iron catalysts are shown in **Figure S7, SM**. As expected, the CO conversion increases with the decrease in GHSV at the same pressure (10 bar). The CO conversion also shows similar trend with increasing the pressure at the same GHSV. Indeed, higher total pressure in the range of 1-20 bar usually results in higher FT reaction rate over iron catalysts. Note however, that the confined iron catalysts show higher CO conversion than the non-confined catalysts under the same reaction conditions. Interestingly, the confined and non-promoted Fe/CNT-in catalyst shows similar activity with the non-confined and promoted FeBi-CNT-out and FePb/CNT out catalysts. Bao [47] et al discovered CO and H<sub>2</sub> enrichment inside the SWCNT tubes based on Monte Carlo simulation. They found that both CO and H<sub>2</sub> were enriched in the pressure range of 1-9 MPa inside the single wall CNT channels. The increased concentration of CO and H<sub>2</sub> could lead to higher reaction rate, while the altered H<sub>2</sub>/CO ratio inside CNTS could also modify the product selectivity. Our results suggest that the observed higher activity over the confined catalysts can be

primarily explained by higher dispersion of iron at the same iron total content when iron is located inside CNT. The TOF seems to be not much affected by iron confinement (**Table 3**). Note that iron dispersion is not affected by the promotion with Bi and Pb but TOF noticeably increases. The strong promotion effect of Bi and Pb might be due to the intimate contact between Fe and promoters [9] inside the CNT. The metallic Bi and Pb have low melting temperature (Bi ~271 °C and Pb ~327 °C) and the promoter migration could therefore occur at the reaction temperature (350 °C). Interestingly, the increase in TOF after the promotion is more significant, when iron nanoparticles are located inside CNT. The promoters inside the tubes may have closer contact with Fe due to the nanoconfinement effect and thus, introduce strong promoting effect on the catalytic performance.

The product distributions observed over the confined and non-confined iron-based catalysts measured as a function of CO conversion are summarized in **Figure 12**. The selectivity to methane and light olefins decreases with increasing CO conversion for the examined catalysts (**Table 3, Figure 12**). More importantly, the confined iron catalysts showed higher selectivity to light olefins compared with the non-confined Fe/CNT-out catalysts at the similar CO conversion levels. The Bi and Pb promoters lead to higher selectivity to light olefins. The selectivities to CO<sub>2</sub> and C<sub>5+</sub> hydrocarbons increase with the CO conversion (**Figure S8, SM**). Higher CO<sub>2</sub> selectivity at higher CO conversion is usually observed over iron FT catalysts and can be relevant to the higher rate of water gas shift reaction due to intensive water production at high CO conversion [48,49]. Higher CO<sub>2</sub> selectivity was observed over

the Bi- and Pb-promoted catalysts compared to the unpromoted catalyst (**Figure S8, SM**). This can be due to the higher rate of carbon monoxide dissociation. In agreement with previous works [9,10], the rate of carbon dioxide dissociation over the promoted catalysts can be enhanced by oxygen scavenging in the presence of the Bi or Pb promoters localized at the interfaces of iron carbide nanoparticles. For a given catalyst, the selectivity to the C<sub>5+</sub> hydrocarbons increases with the conversion. At iso-conversion, the selectivity to the C<sub>5+</sub> hydrocarbons was higher over the unpromoted Fe/CNT-out and Fe/CNT-in catalysts.

A simplified schema of FT reaction consistent with the selectivity variation to different reaction products as a function of carbon monoxide conversion is displayed in **Figure 13**. The schema suggests that CO and hydrogen adsorption on the metal catalysts is followed by formation of the C<sub>1</sub> monomer. Indeed, at very low conversion, the concentration of adsorbed C<sub>1</sub> monomer is very low to enable noticeable polymerization rate. Oligomerization of the C<sub>1</sub> monomers results in formation of the C<sub>2</sub>-C<sub>4</sub> fragments on the catalyst surface. The desorption of these fragments results in light olefins. Hydrogenation of the C<sub>2</sub>-C<sub>4</sub> species leads to light paraffins. Light olefins can readsorb on the catalyst surface. This readsorption can result either in secondary olefin hydrogenation to light paraffins or to further chain growth favoring formation of long-chain C<sub>5+</sub> hydrocarbons. This schema explains the observed decrease in the selectivity to light olefins and increase in the selectivity to the C<sub>5+</sub> hydrocarbons with the CO conversion. Note however, that the Bi and Pb promoters decrease the C<sub>5+</sub> selectivity and the product distribution shifts to lighter hydrocarbons. This is different

compared with alkali promoters [50]. The alkali promoted iron catalysts usually show lower methane selectivity and enhanced selectivity to the C<sub>5+</sub> hydrocarbons.

### 3.2.2. Light olefin synthesis from syngas at atmospheric pressure

Biomass and coal gasification are usually conducted at near atmospheric pressure, while the FT reaction may need higher pressures (10-40 bar). Conducting catalytic reactions at higher pressure requires additional costs, due to gas pressurization. Interestingly and differently to the previously studied iron based FTO catalysts, direct light olefin synthesis from syngas can occur over Bi and Pb-promoted confined catalysts with a high yield even under atmosphere pressure. **Table 4** and **Figure 14** display the CO conversion and light olefin yield over confined and non-confined iron-based catalysts under *iso*-GHSV at atmospheric pressure. The non-promoted and non-confined Fe/CNT-out catalysts exhibit very low CO conversion at atmospheric pressure. The light olefin yield increases only 2-3 times after the promotion with Bi and Pb over Fe/CNT-out non-confined catalyst. The reaction rate over the confined Fe/CNT-in catalyst is higher compared with non-confined one. The 4-5.5 times higher lower olefin yields have been observed on the Bi and Pb promotion of the confined Fe/CNT-in catalyst. After adding a small amount of K (1 wt. %), the catalytic performance is further improved. The resulting FePbK/CNT-in catalyst exhibits around 18 times higher FTY compared with Fe/CNT-out counterpart with the selectivity toward light olefins higher than ~62%.

The catalytic results therefore suggest that the nanoconfinement and promotion produce synergetic effects on the catalytic performance of iron catalysts for FT synthesis both at the reaction pressure of 10 bar and atmospheric pressure. At the same iron content and activation conditions, the effect of nanoconfinement is relevant to the enhancement of iron dispersion, while the intrinsic activity is only slightly affected. The promotion produces stronger effect on the intrinsic activity, while iron dispersion does not change. The nanoconfinement improves the catalytic performance in FT synthesis and the promotion effect is much more pronounced when the iron nanoparticles are located inside the CNT tubes. These confined and promoted catalysts show significant activity even at atmosphere pressure. At 1 bar, the FePb/CNT-in catalyst exhibits the CO conversion 35.9% and light olefin selectivity of 58.9%.

### *3.3 Stability and sintering*

Catalyst deactivation remains one of the main challenges in FT synthesis [51]. The catalyst deactivation in FT reaction is usually an interplay of several phenomena. Some of these phenomena can be reversible and irreversible. Major deactivation mechanisms of iron catalysts involve metal sintering and carbon deposition [2]. **Figure 15** shows carbon monoxide conversion as a function of the reaction time on non-confined and confined monometallic and promoted iron catalysts. The catalyst stability is compared at similar initial carbon monoxide conversion, which was

obtained by adjustment of GHSV. The Fe/CNT-out catalyst shows gradual deactivation during the reaction. The promotion of Fe/CNT-out leading to FeBi/CNT-out and FePb/CNT-out results in a slight improvement of the stability. Much more significant improvement in the stability is observed with the Fe/CNT-in confined catalyst. Moreover, when iron and promoted iron nanoparticles are confined inside the CNT tubes, the resulting catalyst shows no deactivation for more than 100 h (**Figure 15**).

Iron sintering could be one of the reasons of catalyst deactivation. Both the freshly activated and spent catalysts were characterized by TEM. **Figure 16** shows that the size of confined iron particles remains the same after conducting the reaction for 30 h. This indicates that particle sintering is effectively prevented inside CNTs under these reaction conditions. This suggests that nanoconfinement stabilizes iron nanoparticles from sintering. Note that the size of the non-confined nanoparticles in Fe/CNT-out grew to ~15-16 nm after the reaction (**Figure 16, Figure S9, SM**). Even a much stronger sintering was observed over the reference iron catalysts supported by active carbon (Fe/AC). The spent Fe/AC catalysts presents iron nanoparticles of ~24 nm after the catalytic tests (**Figure S2, SM**) compared to 12.1 nm observed in the freshly activated counterpart. The results indicate that nanoconfinement of CNTs facilitates immobilization of the iron species and restricts sintering the growth of iron nanoparticles during the reaction. These results are similar to our previous studies [9,10] of iron catalysts promoted by Bi and Pb and supported over SiO<sub>2</sub> and CNT supports. The CNT nanoconfinement effect for iron particles could restrict sintering.

## 4. Conclusion

Nanoconfinement of iron nanoparticles inside CNT and their promotion with Bi and Pb result in synergetic effects on the structure of iron species and their catalytic performance in light olefin synthesis from syngas. A combination of characterization techniques (TEM, XRD, TPR, synchrotron-based XPS, *in-situ* XANES and *in-situ* magnetic measurements) was indicative of higher iron dispersion in the confined catalysts, while no effect of the promotion on iron particle size was observed. During the catalyst activation in CO, the iron phase transforms from  $\text{Fe}_2\text{O}_3$  to  $\text{Fe}_3\text{O}_4$  and then to the Hägg iron carbide ( $\text{Fe}_5\text{C}_2$ ). The iron reduction and carbidization proceeds much easier for iron species confined inside CNTs and promoted with Bi and Pb. The initial morphology of iron is pod-like structure and it evolves to the core-shell structure with Bi and Pb in the shell during activation and reaction. The nanoconfinement assists in controlling the migration of the promoters by restricting the promoters inside the tubes and thus increase their interaction with iron carbide. The promoting effects and intimate contact of bismuth and lead inside the CNT channels with iron carbides are crucial for obtaining enhanced catalytic performance in high temperature FT synthesis. Both nanoconfinement and promotion with Bi and Pb result in a major increase in FT reaction rates. The increase in FT rate over iron species inside CNT is principally due to the enhancement of iron dispersion, while the promotion with Bi and Pb produces strong effect on intrinsic activity of iron sites. The promotion effect is stronger in the confined catalysts, which is possibly due to the intensive interaction

between the promoter and iron carbides inside CNT. The catalysts containing iron carbide nanoparticles confined inside CNT exhibit high catalytic activity even under atmospheric pressure. The light olefin selectivity is also improved by the promotion and nanoconfinement. Nanoconfinement of iron particles in CNTs slows down iron sintering during the reaction and thus improves the catalyst stability.

## **Acknowledgements**

The authors thank Olivier Gardoll, Laurence Burylo, Pardis Simon and Martine Frère for help with TPR, XRD and XPS measurements. B. G. thanks the China Scholarship Council for providing him a stipend for PhD studies in France. Chevreul Institute (FR 2638), Ministère de l'Enseignement Supérieur, de la Recherche et de l'Innovation, Hauts-de-France Region and FEDER are acknowledged for supporting and funding partially this work. The Laboratório Nacional de Luz Síncrotron (LNLS, Campinas, Brazil) is acknowledged for using the beamtime. The authors acknowledge financial support of the French National Research Agency (NANO4-FUT, Ref. ANR-16-CE06-0013) and from European Union (Interreg V project PSYCHE). GENESIS is supported by the Région Haute-Normandie, the Métropole Rouen Normandie, the CNRS via LABEX EMC and the French National Research Agency as a part of the program "Investissements d'avenir" with the reference ANR-11-EQPX-0020.

## Reference

- [1] H.M. Torres Galvis, J.H. Bitter, C.B. Khare, M. Ruitenbeek, A.I. Dugulan, K.P. de Jong, Supported Iron Nanoparticles as Catalysts for Sustainable Production of Lower Olefins, *Science* (80-. ). 335 (2012) 835–838.  
doi:10.1126/science.1215614.
- [2] H.M. Torres Galvis, K.P. de Jong, Catalysts for Production of Lower Olefins from Synthesis Gas: A Review, *ACS Catal.* 3 (2013) 2130–2149.  
doi:10.1021/cs4003436.
- [3] B. Gu, S. He, W. Zhou, J. Kang, K. Cheng, Q. Zhang, Y. Wang, Polyaniline-supported iron catalyst for selective synthesis of lower olefins from syngas, *J. Energy Chem.* 26 (2017) 608–615.  
doi:10.1016/j.jechem.2017.04.009.
- [4] F. Jiao, J. Li, X. Pan, J. Xiao, H. Li, H. Ma, M. Wei, Y. Pan, Z. Zhou, M. Li, S. Miao, J. Li, Y. Zhu, D. Xiao, T. He, J. Yang, F. Qi, Q. Fu, X. Bao, Selective conversion of syngas to light olefins, *Science* (80-. ). 351 (2016) 1065–1068.  
doi:10.1126/science.aaf1835.
- [5] K. Cheng, B. Gu, X. Liu, J. Kang, Q. Zhang, Y. Wang, Direct and Highly Selective Conversion of Synthesis Gas into Lower Olefins: Design of a Bifunctional Catalyst Combining Methanol Synthesis and Carbon-Carbon Coupling, *Angew. Chemie Int. Ed.* 55 (2016) 4725–4728.

- doi:10.1002/anie.201601208.
- [6] D.B. Bukur, D. Mukesh, S.A. Patel, Promoter effects on precipitated iron catalysts for Fischer-Tropsch synthesis, *Ind. Eng. Chem. Res.* 29 (1990) 194–204. doi:10.1021/ie00098a008.
- [7] H. Arakawa, A.T. Bell, Effects of potassium promotion on the activity and selectivity of iron Fischer-Tropsch catalysts, *Ind. Eng. Chem. Process Des. Dev.* 22 (1983) 97–103. doi:10.1021/i200020a017.
- [8] J. Xie, J. Yang, A.I. Dugulan, A. Holmen, D. Chen, K.P. de Jong, M.J. Louwse, Size and Promoter Effects in Supported Iron Fischer–Tropsch Catalysts: Insights from Experiment and Theory, *ACS Catal.* 6 (2016) 3147–3157. doi:10.1021/acscatal.6b00131.
- [9] B. Gu, V.V. Ordonsky, M. Bahri, O. Ersen, P.A. Chernavskii, D. Filimonov, A.Y. Khodakov, Effects of the promotion with bismuth and lead on direct synthesis of light olefins from syngas over carbon nanotube supported iron catalysts, *Appl. Catal. B Environ.* 234 (2018). doi:10.1016/j.apcatb.2018.04.025.
- [10] V.V. Ordonsky, Y. Luo, B. Gu, A. Carvalho, P.A. Chernavskii, K. Cheng, A.Y. Khodakov, Soldering of iron catalysts for direct synthesis of light olefins from syngas under mild reaction conditions, *ACS Catal.* 7 (2017). doi:10.1021/acscatal.7b01307.
- [11] Z. Yang, X. Pan, J. Wang, X. Bao, FeN particles confined inside CNT for light olefin synthesis from syngas: Effects of Mn and K additives, *Catal. Today.* 186

- (2012) 121–127. doi:10.1016/j.cattod.2011.11.034.
- [12] G. Yu, B. Sun, Y. Pei, S. Xie, S. Yan, M. Qiao, K. Fan, X. Zhang, B. Zong, Fe x O y @C Spheres as an Excellent Catalyst for Fischer–Tropsch Synthesis, *J. Am. Chem. Soc.* 132 (2010) 935–937. doi:10.1021/ja906370b.
- [13] H. Qin, B. Wang, C. Zhang, B. Zhu, Y. Zhou, Q. Zhou, Lignin based synthesis of graphitic carbon-encapsulated iron nanoparticles as effective catalyst for forming lower olefins via Fischer-Tropsch synthesis, *Catal. Commun.* 96 (2017) 28–31. doi:10.1016/j.catcom.2017.03.022.
- [14] Z. Sun, B. Sun, M. Qiao, J. Wei, Q. Yue, C. Wang, Y. Deng, S. Kaliaguine, D. Zhao, A General Chelate-Assisted Co-Assembly to Metallic Nanoparticles-Incorporated Ordered Mesoporous Carbon Catalysts for Fischer–Tropsch Synthesis, *J. Am. Chem. Soc.* 134 (2012) 17653–17660. doi:10.1021/ja306913x.
- [15] H. Qin, S. Kang, Y. Wang, H. Liu, Z. Ni, Y. Huang, Y. Li, X. Li, Lignin-Based Fabrication of Co@C Core–Shell Nanoparticles as Efficient Catalyst for Selective Fischer–Tropsch Synthesis of C 5+ Compounds, *ACS Sustain. Chem. Eng.* 4 (2016) 1240–1247. doi:10.1021/acssuschemeng.5b01269.
- [16] Y. Cao, M. Lu, J. Fang, L. Shi, D. Zhang, Hexagonal boron nitride supported mesoSiO 2 -confined Ni catalysts for dry reforming of methane, *Chem. Commun.* 53 (2017) 7549–7552. doi:10.1039/C7CC02007D.
- [17] X. Yang, W. Wang, L. Wu, X. Li, T. Wang, S. Liao, Effect of confinement of TiO 2 nanotubes over the Ru nanoparticles on Fischer-Tropsch synthesis, *Appl.*

- Catal. A Gen. 526 (2016) 45–52. doi:10.1016/j.apcata.2016.07.021.
- [18] X. Pan, Z. Fan, W. Chen, Y. Ding, H. Luo, X. Bao, Enhanced ethanol production inside carbon-nanotube reactors containing catalytic particles, *Nat. Mater.* 6 (2007) 507–511. doi:10.1038/nmat1916.
- [19] P. Serp, E. Castillejos, Catalysis in Carbon Nanotubes, *ChemCatChem.* 2 (2010) 41–47. doi:10.1002/cctc.200900283.
- [20] W. Chen, Z. Fan, X. Pan, X. Bao, Effect of Confinement in Carbon Nanotubes on the Activity of Fischer–Tropsch Iron Catalyst, *J. Am. Chem. Soc.* 130 (2008) 9414–9419. doi:10.1021/ja8008192.
- [21] W. Chen, X. Pan, X. Bao, Tuning of Redox Properties of Iron and Iron Oxides via Encapsulation within Carbon Nanotubes, *J. Am. Chem. Soc.* 129 (2007) 7421–7426. doi:10.1021/ja0713072.
- [22] X. Chen, D. Deng, X. Pan, X. Bao, Iron catalyst encapsulated in carbon nanotubes for CO hydrogenation to light olefins, *Chinese J. Catal.* 36 (2015) 1631–1637. doi:10.1016/S1872-2067(15)60882-8.
- [23] Z. Yang, S. Guo, X. Pan, J. Wang, X. Bao, FeN nanoparticles confined in carbon nanotubes for CO hydrogenation, *Energy Environ. Sci.* 4 (2011) 4500. doi:10.1039/c1ee01428e.
- [24] J. Xiao, X. Pan, S. Guo, P. Ren, X. Bao, Toward Fundamentals of Confined Catalysis in Carbon Nanotubes, *J. Am. Chem. Soc.* 137 (2015) 477–482. doi:10.1021/ja511498s.
- [25] B. Gu, C. Zhou, S. He, S. Moldovan, P.A. Chernavskii, V. V. Ordonsky, A.Y.

- Khodakov, Size and promoter effects on iron nanoparticles confined in carbon nanotubes and their catalytic performance in light olefin synthesis from syngas, *Catal. Today*. (2019). doi:10.1016/j.cattod.2019.05.054.
- [26] P.A. Chernavskii, A.Y. Khodakov, G.V. Pankina, J.-S. Girardon, E. Quinet, In situ characterization of the genesis of cobalt metal particles in silica-supported Fischer-Tropsch catalysts using Foner magnetic method, *Appl. Catal. A Gen.* 306 (2006). doi:10.1016/j.apcata.2006.03.033.
- [27] P.A. Chernavskii, J.-A. Dalmon, N.S. Perov, A.Y. Khodakov, Magnetic characterization of Fischer-Tropsch catalysts, *Oil Gas Sci. Technol.* 64 (2009). doi:10.2516/ogst/2008050.
- [28] V.K. Jones, L.R. Neubauer, C.H. Bartholomew, Effects of crystallite size and support on the carbon monoxide hydrogenation activity/selectivity properties of iron/carbon, *J. Phys. Chem.* 90 (1986) 4832–4839. doi:10.1021/j100411a023.
- [29] H.M. Torres Galvis, J.H. Bitter, T. Davidian, M. Ruitenbeek, A.I. Dugulan, K.P. de Jong, Iron Particle Size Effects for Direct Production of Lower Olefins from Synthesis Gas, *J. Am. Chem. Soc.* 134 (2012) 16207–16215. doi:10.1021/ja304958u.
- [30] A.-H. Lu, X. Bao, Carbon in the Catalysis Community, *ChemCatChem*. 7 (2015) 2724–2725. doi:10.1002/cctc.201500953.
- [31] G. Jacobs, W. Ma, P. Gao, B. Todic, T. Bhatelia, D.B. Bukur, B.H. Davis, The application of synchrotron methods in characterizing iron and cobalt Fischer–Tropsch synthesis catalysts, *Catal. Today*. 214 (2013) 100–139.

- doi:10.1016/j.cattod.2013.05.011.
- [32] L. Sciortino, A. Alessi, F. Messina, G. Buscarino, F.M. Gelardi, Structure of the FeBTC Metal–Organic Framework: A Model Based on the Local Environment Study, *J. Phys. Chem. C*. 119 (2015) 7826–7830.  
doi:10.1021/acs.jpcc.5b01336.
- [33] X. Pan, X. Bao, The Effects of Confinement inside Carbon Nanotubes on Catalysis, *Acc. Chem. Res.* 44 (2011) 553–562. doi:10.1021/ar100160t.
- [34] C. Wang, X. Pan, X. Bao, Direct production of light olefins from syngas over a carbon nanotube confined iron catalyst, *Chinese Sci. Bull.* 55 (2010) 1117–1119. doi:10.1007/s11434-010-0076-8.
- [35] Q. Cheng, Y. Tian, S. Lyu, N. Zhao, K. Ma, T. Ding, Z. Jiang, L. Wang, J. Zhang, L. Zheng, F. Gao, L. Dong, N. Tsubaki, X. Li, Confined small-sized cobalt catalysts stimulate carbon-chain growth reversely by modifying ASF law of Fischer–Tropsch synthesis, *Nat. Commun.* 9 (2018) 3250.  
doi:10.1038/s41467-018-05755-8.
- [36] K. Mai, T. Elder, L.H. Groom, J.J. Spivey, Fe-based Fischer Tropsch synthesis of biomass-derived syngas: Effect of synthesis method, *Catal. Commun.* 65 (2015) 76–80. doi:10.1016/j.catcom.2015.02.027.
- [37] V. Subramanian, V. V. Ordonsky, B. Legras, K. Cheng, C. Cordier, P.A. Chernavskii, A.Y. Khodakov, Design of iron catalysts supported on carbon–silica composites with enhanced catalytic performance in high-temperature Fischer–Tropsch synthesis, *Catal. Sci. Technol.* 6 (2016) 4953–4961.

- doi:10.1039/C6CY00060F.
- [38] R.M.M. Abbaslou, A. Tavassoli, J. Soltan, A.K. Dalai, Iron catalysts supported on carbon nanotubes for Fischer–Tropsch synthesis: Effect of catalytic site position, *Appl. Catal. A Gen.* 367 (2009) 47–52.  
doi:10.1016/j.apcata.2009.07.025.
- [39] T. Li, Y. Yang, C. Zhang, X. An, H. Wan, Z. Tao, H. Xiang, Y. Li, F. Yi, B. Xu, Effect of manganese on an iron-based Fischer–Tropsch synthesis catalyst prepared from ferrous sulfate, *Fuel.* 86 (2007) 921–928.  
doi:10.1016/j.fuel.2006.10.019.
- [40] P.A. Chernavskii, V.O. Kazak, G.V. Pankina, V.V. Ordonsky, A.Y. Khodakov, Mechanistic aspects of the activation of silica-supported iron catalysts for Fischer-Tropsch synthesis in carbon monoxide and syngas, *ChemCatChem.* 8 (2016). doi:10.1002/cctc.201500811.
- [41] A. Jean-Marie, A. Griboval-Constant, A.Y. Khodakov, F. Diehl, Influence of sub-stoichiometric sorbitol addition modes on the structure and catalytic performance of alumina-supported cobalt Fischer-Tropsch catalysts, *Catal. Today.* 171 (2011). doi:10.1016/j.cattod.2011.04.002.
- [42] S. Li, G.D. Meitzner, E. Iglesia, Structure and Site Evolution of Iron Oxide Catalyst Precursors during the Fischer–Tropsch Synthesis, *J. Phys. Chem. B.* 105 (2001) 5743–5750. doi:10.1021/jp010288u.
- [43] S. Abelló, D. Montané, Exploring Iron-based Multifunctional Catalysts for Fischer-Tropsch Synthesis: A Review, *ChemSusChem.* 4 (2011) 1538–1556.

- doi:10.1002/cssc.201100189.
- [44] E. de Smit, B.M. Weckhuysen, The renaissance of iron-based Fischer–Tropsch synthesis: on the multifaceted catalyst deactivation behaviour, *Chem. Soc. Rev.* 37 (2008) 2758. doi:10.1039/b805427d.
- [45] J.B. Butt, Carbide phases on iron-based Fischer-Tropsch synthesis catalysts part I: Characterization studies, *Catal. Letters.* 7 (1991) 61–81. doi:10.1007/BF00764492.
- [46] K. Cheng, V.V. Ordonsky, M. Virginie, B. Legras, P.A. Chernavskii, V.O. Kazak, C. Cordier, S. Paul, Y. Wang, A.Y. Khodakov, Support effects in high temperature Fischer-Tropsch synthesis on iron catalysts, *Appl. Catal. A Gen.* 488 (2014) 66–77. doi:10.1016/j.apcata.2014.09.033.
- [47] J. Guan, X. Pan, X. Liu, X. Bao, Syngas Segregation Induced by Confinement in Carbon Nanotubes: A Combined First-Principles and Monte Carlo Study, *J. Phys. Chem. C.* 113 (2009) 21687–21692. doi:10.1021/jp906092c.
- [48] W. Ngantsoue-Hoc, Y. Zhang, R.J. O’Brien, M. Luo, B.H. Davis, Fischer–Tropsch synthesis: activity and selectivity for Group I alkali promoted iron-based catalysts, *Appl. Catal. A Gen.* 236 (2002) 77–89. doi:10.1016/S0926-860X(02)00278-8.
- [49] H. Xiong, M.A. Motchelaho, M. Moyo, L.L. Jewell, N.J. Coville, Effect of Group I alkali metal promoters on Fe/CNT catalysts in Fischer–Tropsch synthesis, *Fuel.* 150 (2015) 687–696. doi:10.1016/j.fuel.2015.02.099.
- [50] K. Cheng, V. V. Ordonsky, B. Legras, M. Virginie, S. Paul, Y. Wang, A.Y.

Khodakov, Sodium-promoted iron catalysts prepared on different supports for high temperature Fischer–Tropsch synthesis, *Appl. Catal. A Gen.* 502 (2015) 204–214. doi:10.1016/j.apcata.2015.06.010.

- [51] C.H. Bartholomew, Mechanisms of catalyst deactivation, *Appl. Catal. A Gen.* 212 (2001) 17–60. doi:10.1016/S0926-860X(00)00843-7.

**Table 1.** Physical properties of supports and supported Fe catalysts.

Sample	$S_{\text{BET}}^{\text{a}}$ ( $\text{m}^2/\text{g}$ )	$V_{\text{tot}}^{\text{b}}$ ( $\text{cm}^3/\text{g}$ )	$D_{\text{meso}}^{\text{c}}$ (nm)	$D_{\text{metal}}^{\text{d}}$ (nm)	$D_{\text{metal}}^{\text{e}}$ (nm)	Total $\text{H}_2$ consumption <sup>f</sup> (mmol/g)	Fe content <sup>g</sup> (wt%)	Bi or Pb content <sup>g</sup> (wt%)
CNT-close	153.3	0.54	15.4	-	-	-	-	-
Fe/CNT-out	141.4	0.52	14.7	10.2	9.3	1.5	10.2	-
FeBi/CNT-out	134.7	0.52	15.3	9.6	8.9	1.7	10.4	0.84
FePb/CNT-out	128.3	0.52	16.3	10.3	9.5	1.6	10.6	0.82
CNT-open	230.3	0.83	14.4	-	-	-	-	-
Fe/CNT-in	192.9	0.52	10.8	5.3	4.9	1.6	10.3	-
FeBi/CNT-in	183.3	0.52	11.3	5.6	5.1	2.1	10.5	0.83
FePb/CNT-in	187.8	0.50	10.2	5.8	5.3	1.9	10.9	0.85

<sup>a</sup>BET surface area.

<sup>b</sup> Single point desorption total pore volume of pores,  $P/P_0=0.975$ .

<sup>c</sup> The pore diameter in the mesoporous region evaluated by the BJH method.

<sup>d</sup> Average particle size of iron oxide by XRD.

<sup>e</sup> Average particle size of iron oxide by TEM.

<sup>f</sup> The total  $\text{H}_2$  consumption and iron reducibility degree from TPR analysis.

<sup>g</sup> The Fe, Bi and Pb content from ICP-OES.

**Table 2.** Iron and bismuth phase evolution of the fresh catalysts, activated catalysts and used catalysts by in-situ XANES (CO activation at 350 °C for 90 min, reaction in syngas at 350 °C for 90 min)

Catalysts	Fresh (%)		CO activation (%)			Reaction in syngas (%)		
Fe XANES								
	Fe <sub>2</sub> O <sub>3</sub>	Fe <sub>3</sub> O <sub>4</sub>	Fe <sub>2</sub> O <sub>3</sub>	Fe <sub>3</sub> O <sub>4</sub>	Fe <sub>x</sub> C <sub>y</sub>	Fe <sub>2</sub> O <sub>3</sub>	Fe <sub>3</sub> O <sub>4</sub>	Fe <sub>x</sub> C <sub>y</sub>
Fe/CNT-out	48.4	51.6	10.3	22.3	67.4	5.2	19.7	75.1
FeBi/CNT-out	45.1	54.9	0	14.4	85.6	0	8.7	91.3
FeBi/CNT-in	38.6	61.4	0	0	100	0.1	0.2	99.7
Bi XANES								
	Bi <sub>2</sub> O <sub>3</sub>		Bi <sub>2</sub> O <sub>3</sub>		Bi	Bi <sub>2</sub> O <sub>3</sub>		Bi
FeBi/CNT-out	100		0		100	0.9		99.1
FeBi/CNT-in	100		0		100	1.1		98.9

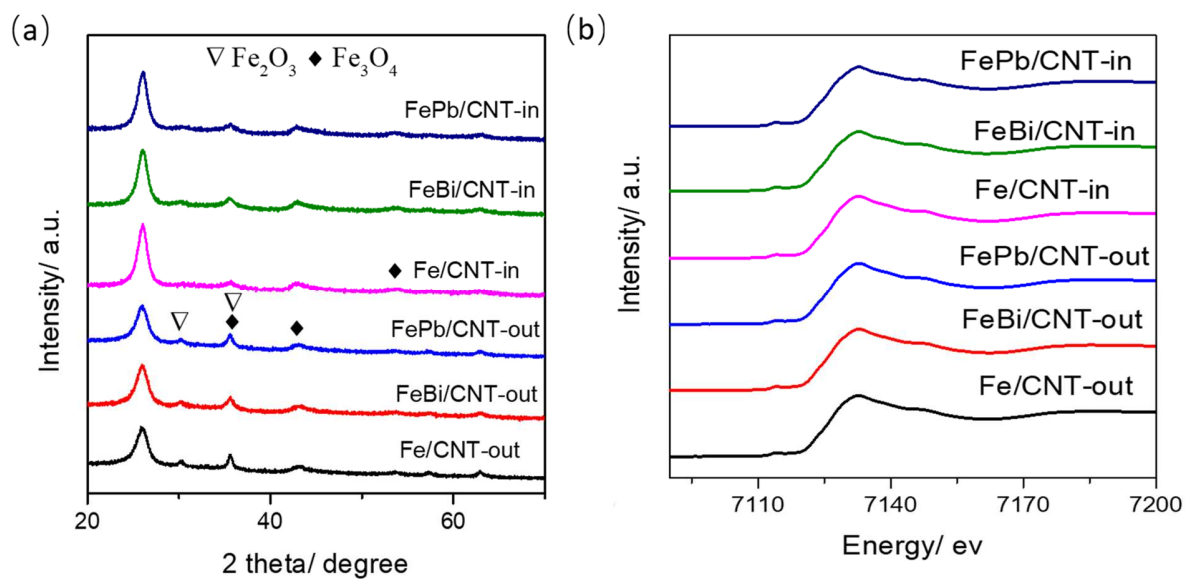
**Table 3.** Catalytic performance of non-confined and confined iron catalysts in FT synthesis (10 bar, 350 °C, H<sub>2</sub>/CO = 1/1, GHSV = 17 L/g.h, TOS = 10h)

Catalysts	FTY 10 <sup>-4</sup> molCOg <sub>Fe</sub> <sup>-1</sup> h <sup>-1</sup>	TOF (s <sup>-1</sup> )	CO conv. (%)	CO <sub>2</sub> select. (%)	Hydrocarbon selectivity (%)				C <sub>2-4</sub> <sup>=</sup> / C <sub>2-4</sub> <sup>0</sup>
					CH <sub>4</sub>	C <sub>2-4</sub> <sup>=</sup>	C <sub>2-4</sub> <sup>0</sup>	C <sub>5</sub> <sup>+</sup>	
Fe/AC	0.8	0.282	8.0	28.8	35.6	28.2	22.9	13.3	1.23
Fe/CNT-out	1.6	0.436	14.4	30.4	34.2	32.4	18.4	15.0	1.76
FeBi/CNT-out	3.3	0.862	28.9	38.8	32.3	37.5	16.0	14.2	2.34
FePb/CNT-out	3.9	1.080	34.3	41.1	30.8	35.3	17.4	14.5	2.03
Fe/CNT-in	2.8	0.403	24.8	39.9	28.5	36.9	13.8	20.8	2.67
FeBi/CNT-in	6.9	1.033	60.2	45.2	25.5	45.0	12.0	17.5	3.75
FePb/CNT-in	8.2	1.276	71.0	47.4	25	40.7	14.6	19.7	2.79
FePb/CNT-in*	23.4	-	45.0	39.4	26.1	41.0	15.9	17.0	2.58
FePbK/CNT-in	8.8	-	76.2	48.1	18.2	52.6	8.6	21.0	6.12

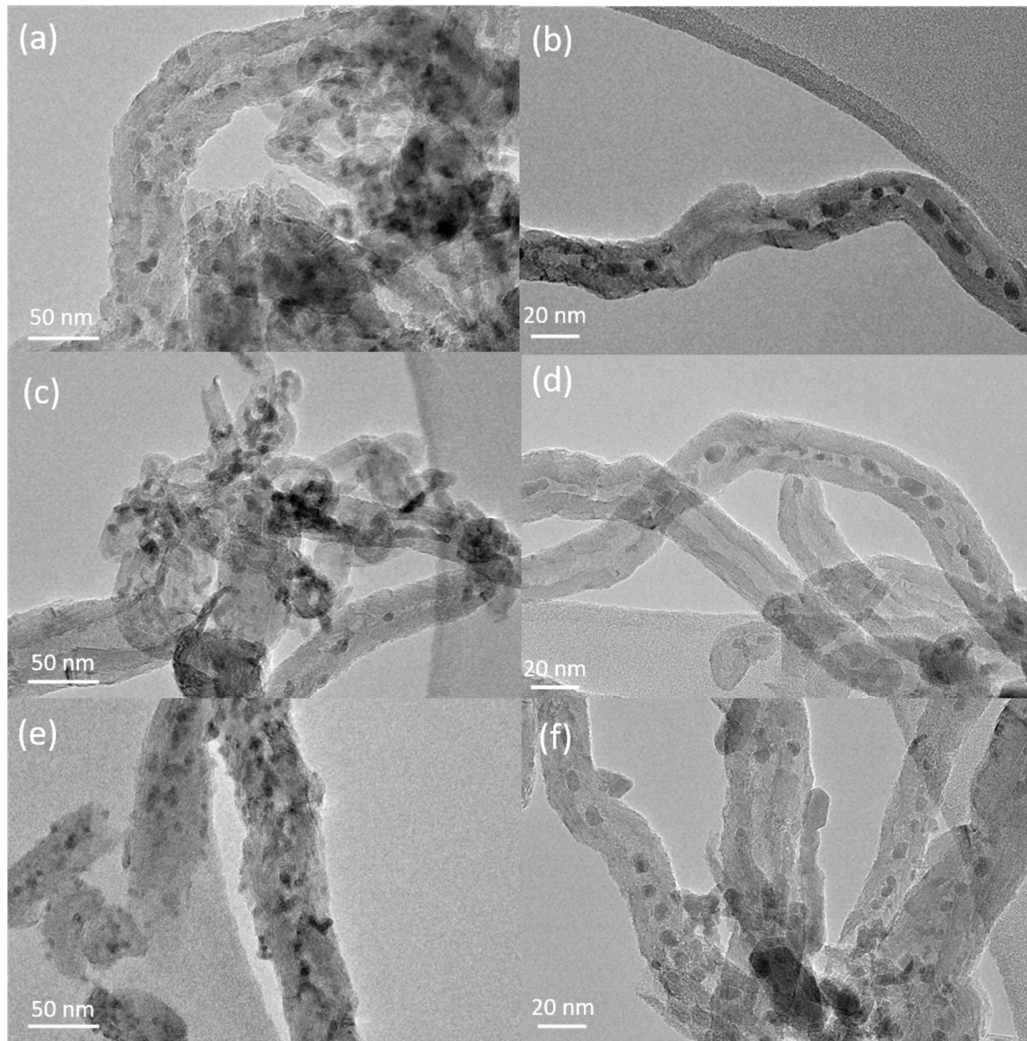
\*P = 20 bar, T = 350 °C, GHSV = 84 L/g.h

**Table 4.** Catalytic performance of non-confined and confined iron catalysts in FT synthesis (1 bar, 350 °C, H<sub>2</sub>/CO = 1/1, GHSV = 3.4 L/g.h, TOS = 10 h)

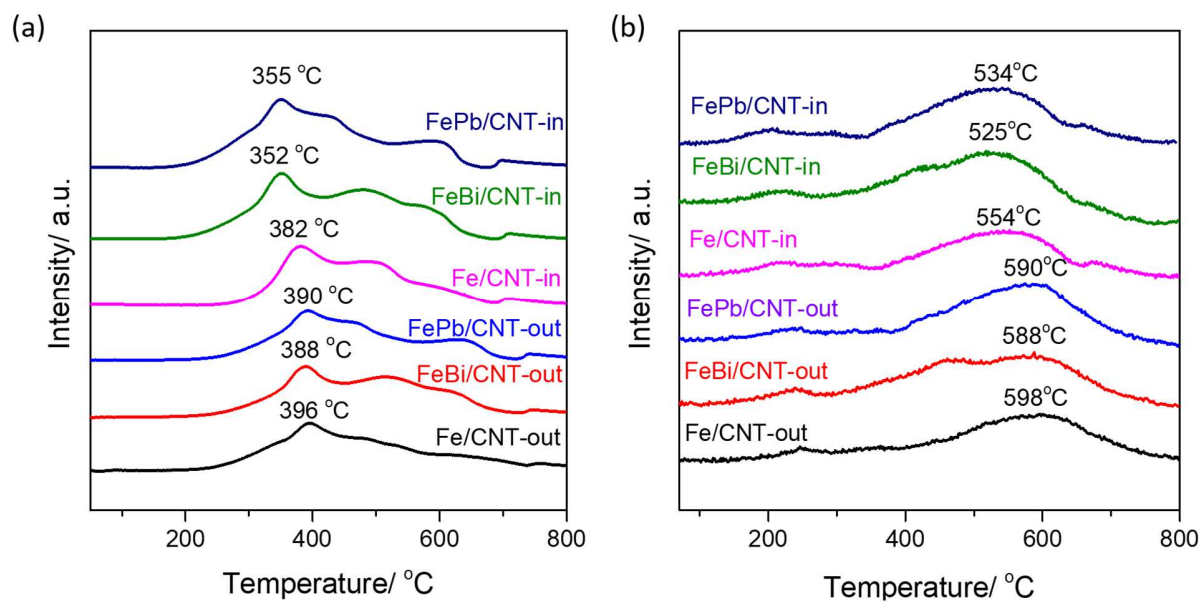
Catalysts	FTY 10 <sup>-5</sup> mol <sub>CO</sub> g <sub>Fe</sub> <sup>-1</sup> s <sup>-1</sup>	CO conv. (%)	CO <sub>2</sub> select. (%)	Hydrocarbon selectivity (%)				C <sub>2-4</sub> <sup>=</sup> / C <sub>2-4</sub> <sup>0</sup>
				CH <sub>4</sub>	C <sub>2-4</sub> <sup>=</sup>	C <sub>2-4</sub> <sup>0</sup>	C <sub>5</sub> <sup>+</sup>	
Fe/AC	0.5	2.5	18.7	40.3	34.4	18.7	6.6	1.84
Fe/CNT-out	0.8	4.3	20.2	37.3	35.2	18.9	11.6	1.86
FeBi/CNT-out	1.6	8.5	25.8	31.5	47.6	12.7	8.2	3.75
FePb/CNT-out	2.4	12.9	30.5	30.9	44.9	15.2	9.0	2.95
Fe/CNT-in	1.5	8.0	29.2	31.9	40.4	11.7	16.0	3.45
FeBi/CNT-in	4.7	25.6	37.3	27.0	62.4	6.5	4.6	9.60
FePb/CNT-in	6.6	35.9	39.9	26.1	58.9	7.4	7.6	7.96
FePbK/CNT-in	7.5	40.7	42.4	19.2	62.0	6.1	12.7	10.2



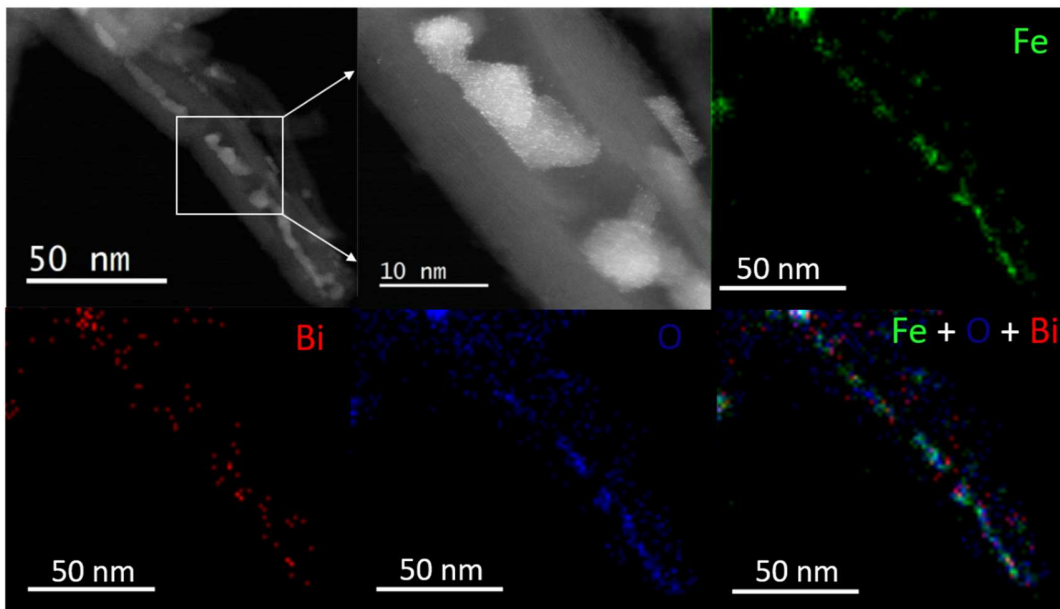
**Figure 1.** Structural characterization of the catalysts. (a) XRD profiles of the confined and non-confined iron-based catalysts, (b) Normalized XAS of Fe L-edge of the Fe/CNT-out and Fe/CNT-in based catalysts.



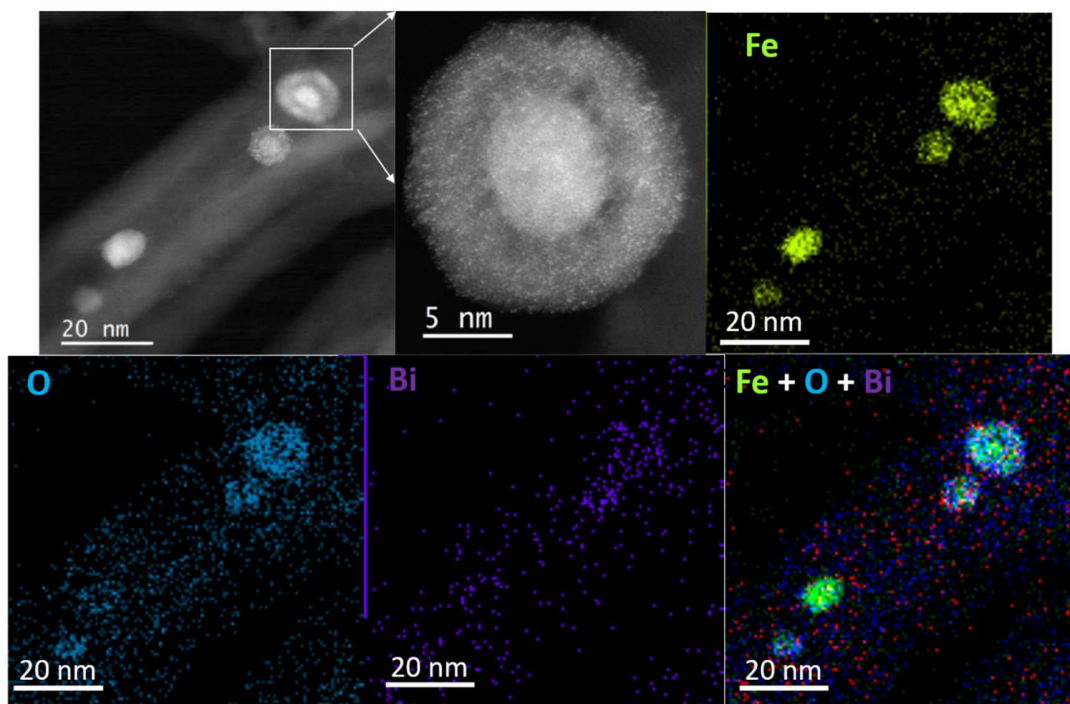
**Figure 2.** TEM micrographs for fresh confined and non-confined Fe catalysts: (a) Fe/CNT-out, (b) Fe/CNT-in, (c) FeBi/CNT-out, (d) FeBi/CNT-in, (e) FePb/CNT-out, (e) FePb/CNT-in.



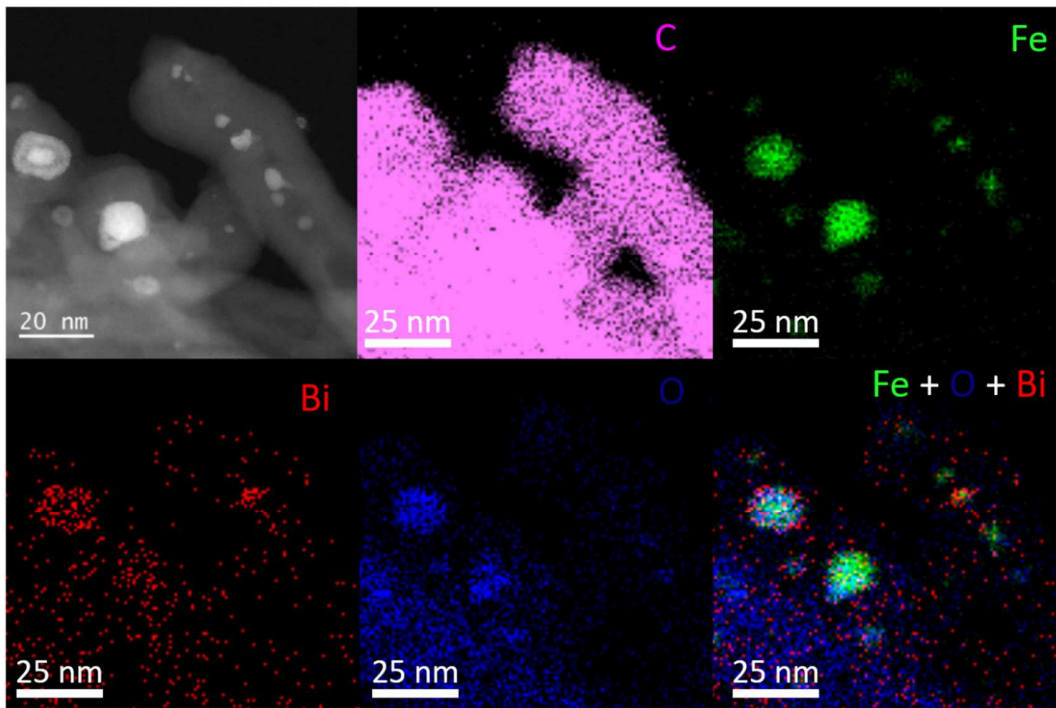
**Figure 3.** TPR profiles of the confined and non-confined iron-based catalysts. (a) H<sub>2</sub>-TPR, (b) CO-TPR.



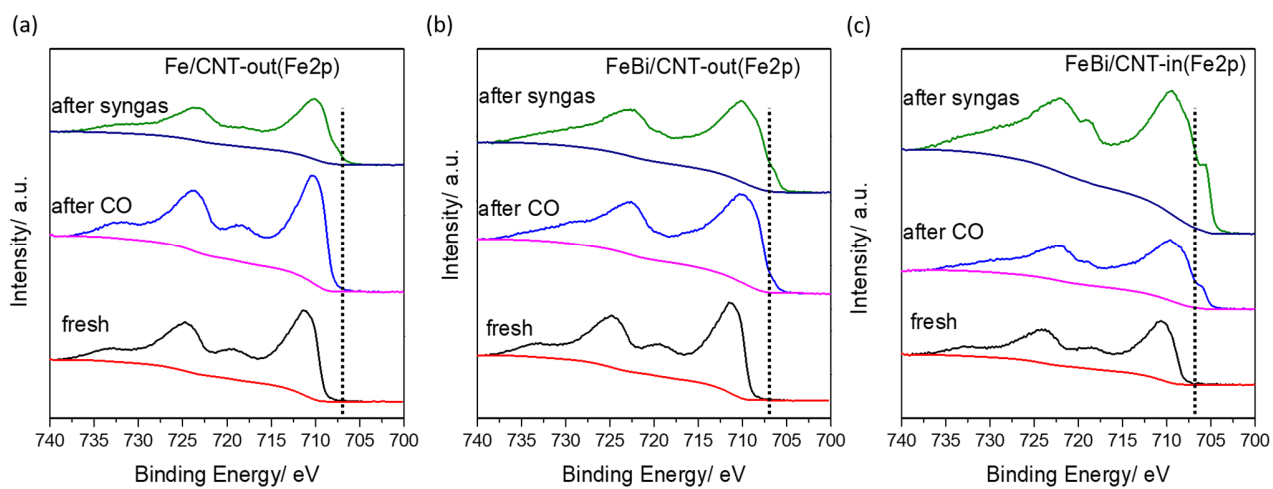
**Figure 4.** STEM-HAADF images and STEM-EDX elemental maps of the FeBi/CNT-in fresh catalyst.



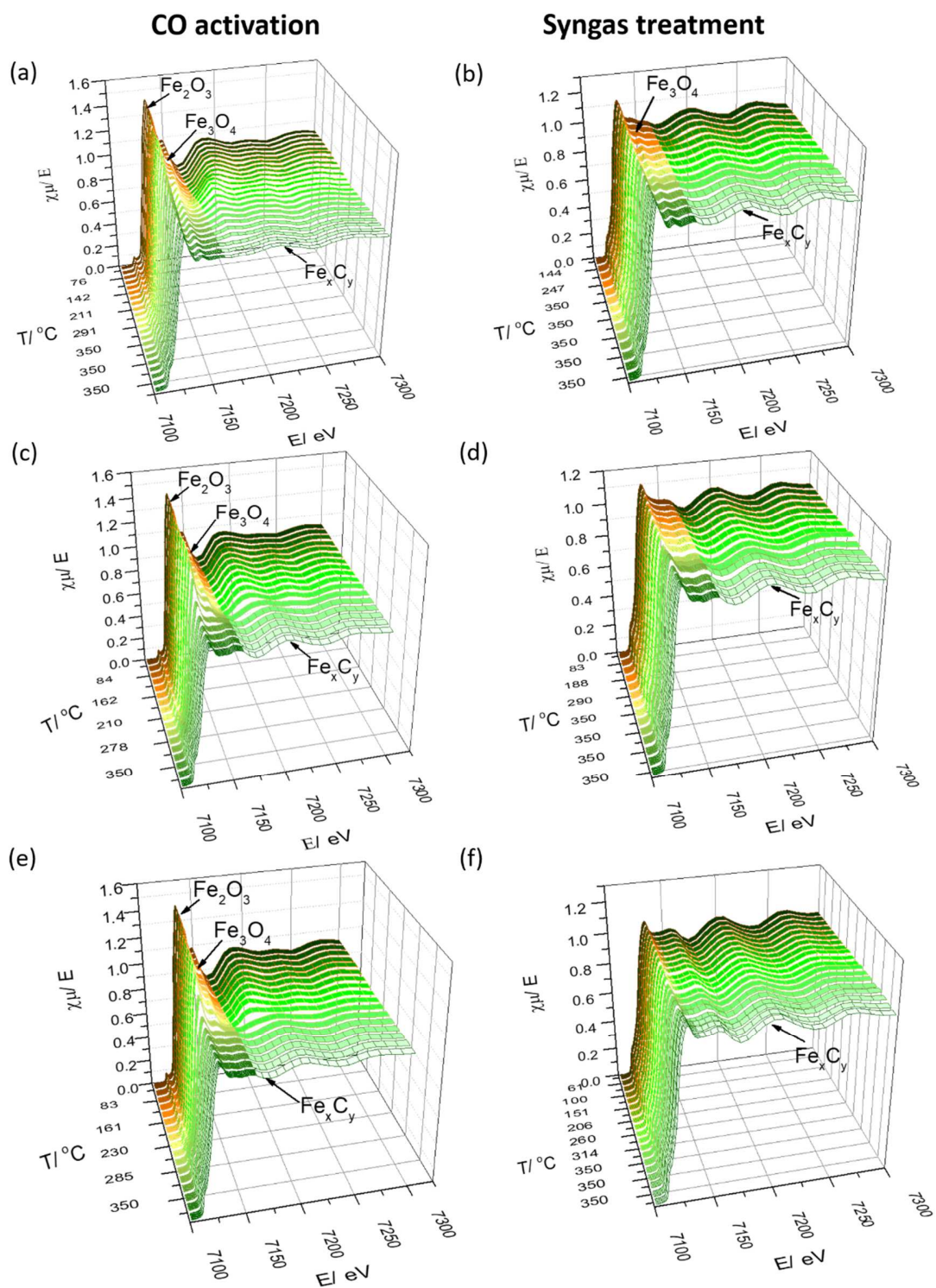
**Figure 5.** High Resolution STEM-HAADF micrographs and STEM-EDX elemental maps of the activated FeBi/CNT-in catalyst (CO treatment for 10 h at 350 °C).



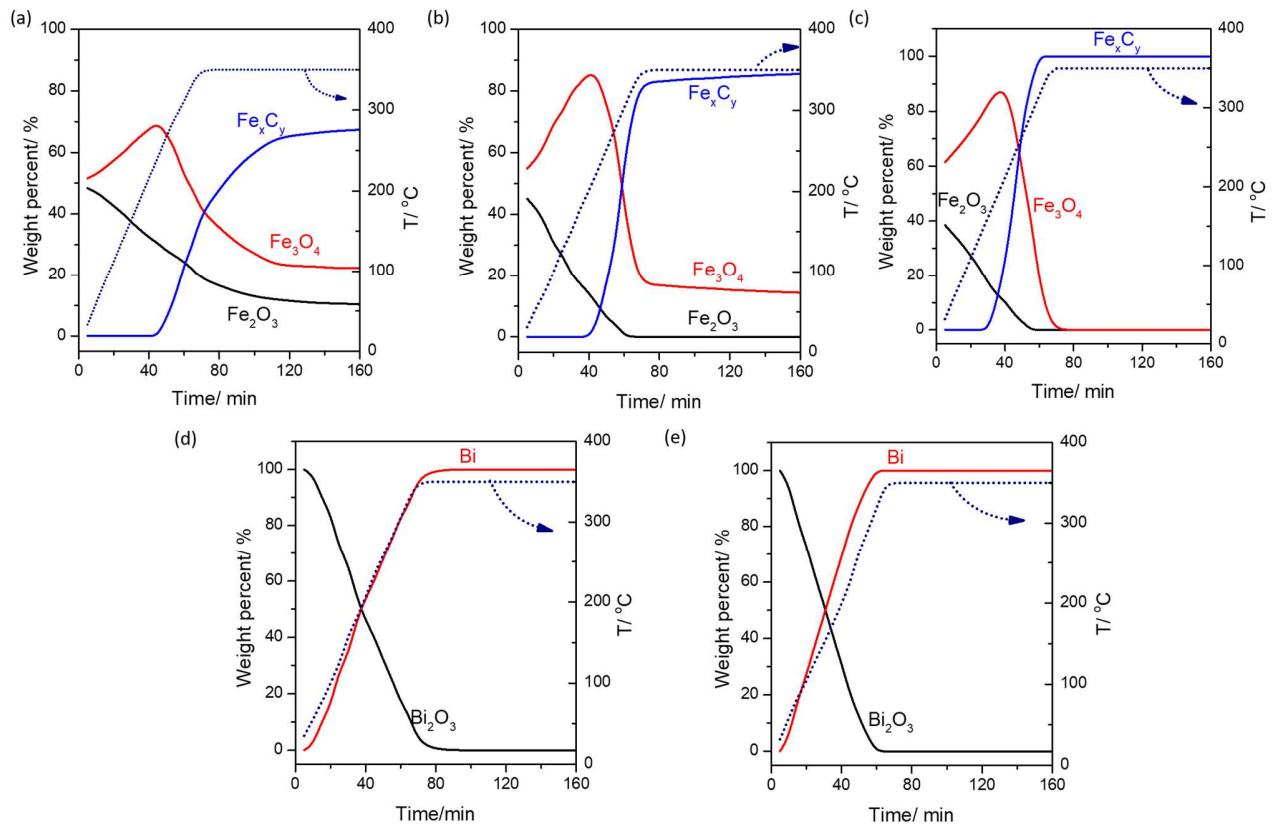
**Figure 6.** STEM-HAADF image and STEM-EDX elemental maps of the spent FeBi/CNT-in catalyst (after the catalytic test).



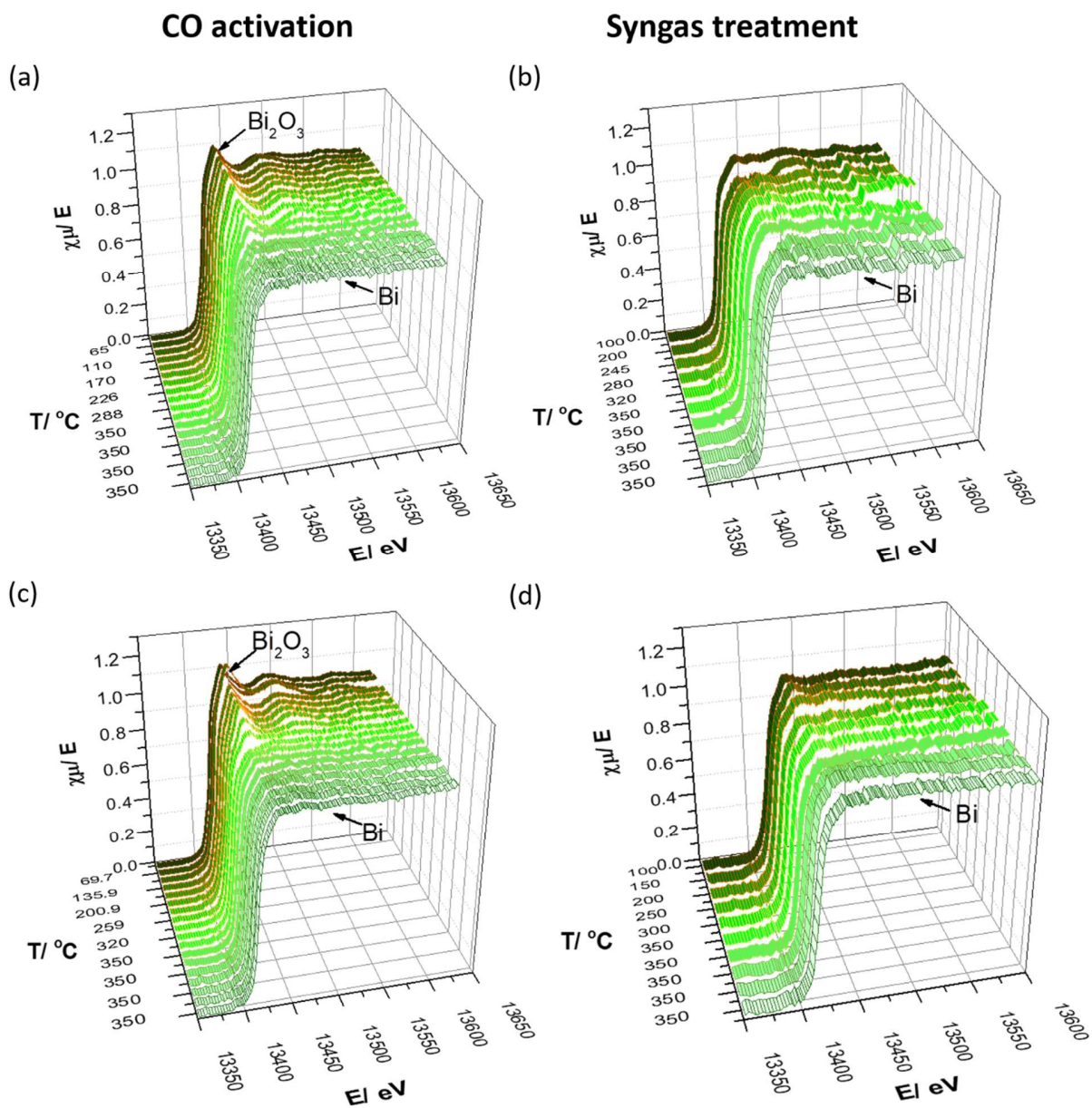
**Figure 7.** Fe 2p XPS of the catalysts after calcination, exposure to carbon monoxide and syngas. (a) Fe/CNT-out, (b) FeBi/CNT-out, (c) FeBi/CNT-in.



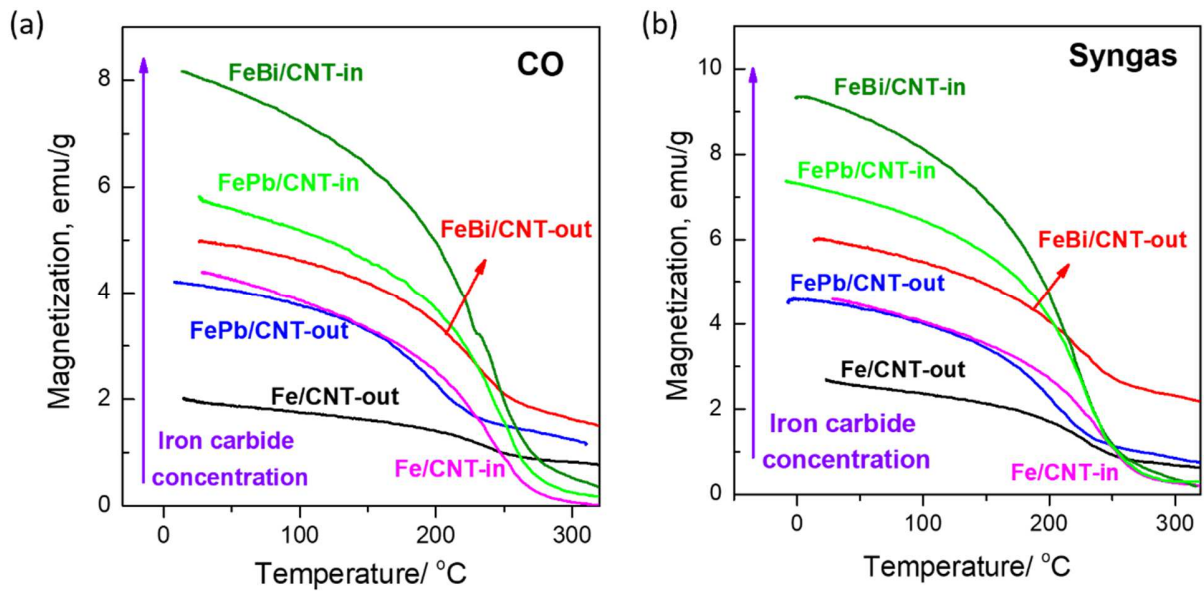
**Figure 8.** Fe K-edge XANES spectra of the temperature-programmed carbonization and reaction of the non-confined and confined iron-based catalysts. Temperature ranged from 30 to 350 °C. (a) and (b) Fe/CNT-out, (c) and (d) FeBi/CNT-out, (e) and (f) FeBi/CNT-in.



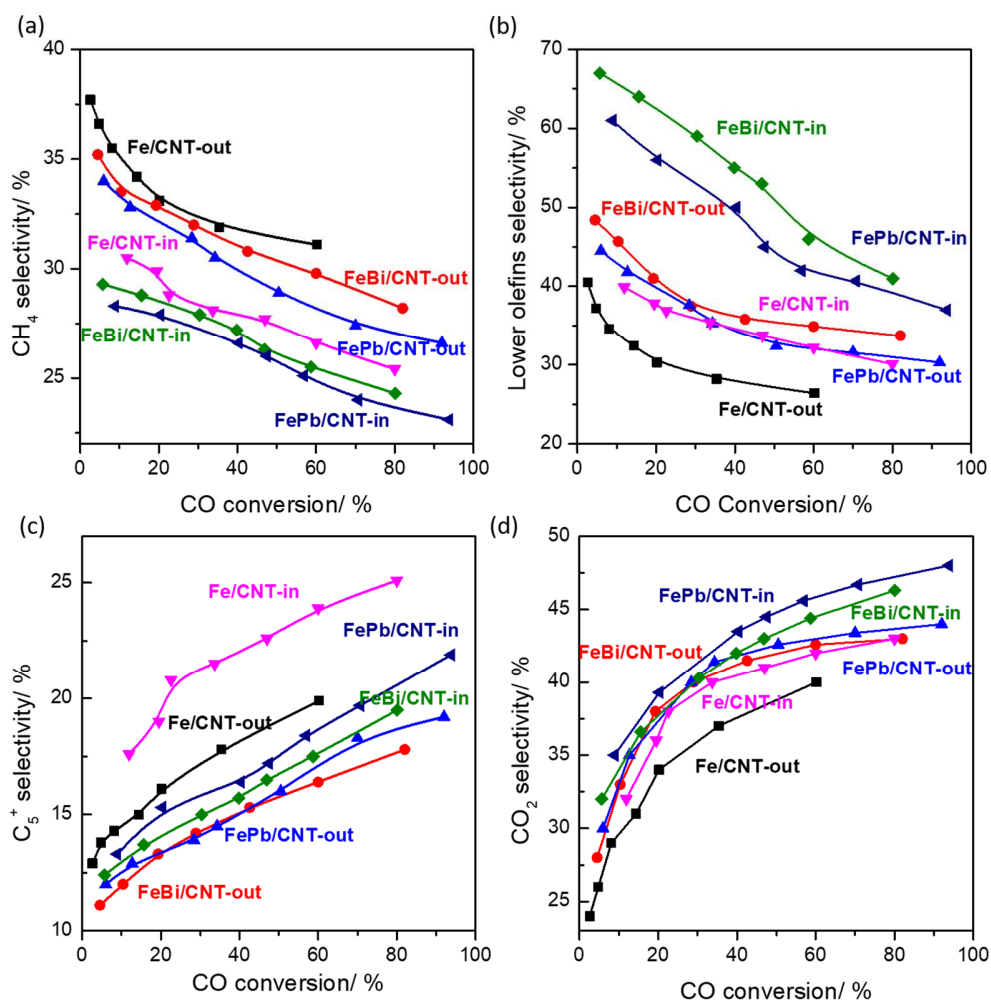
**Figure 9.** Linear combination fitting of XANES for iron and bismuth phase evolution during activation in CO: (a) Fe/CNT-out, (b) and (d) FeBi/CNT-out, (c) and (e) FeBi/CNT-in.



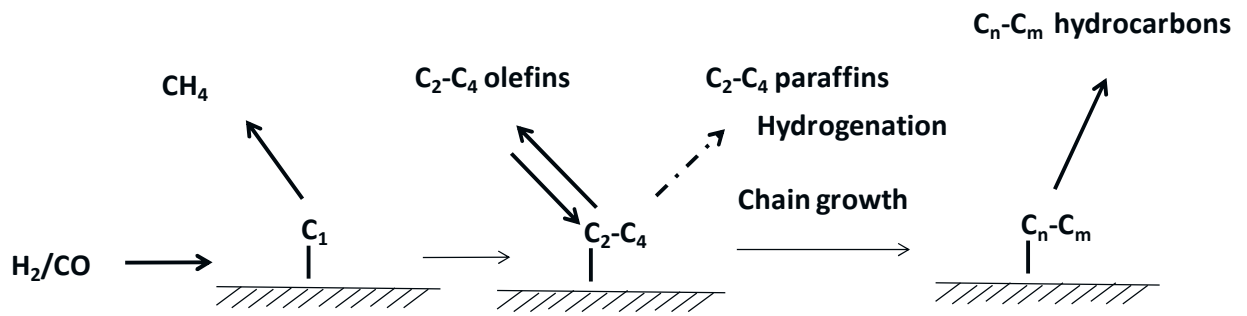
**Figure 10.** Bi L<sub>3</sub>-edge XANES spectra of the temperature-programmed carbonization and reaction of the non-confined and confined iron-based catalysts. (a) and (b) FeBi/CNT-out, (c) and (d) FeBi/CNT-in.



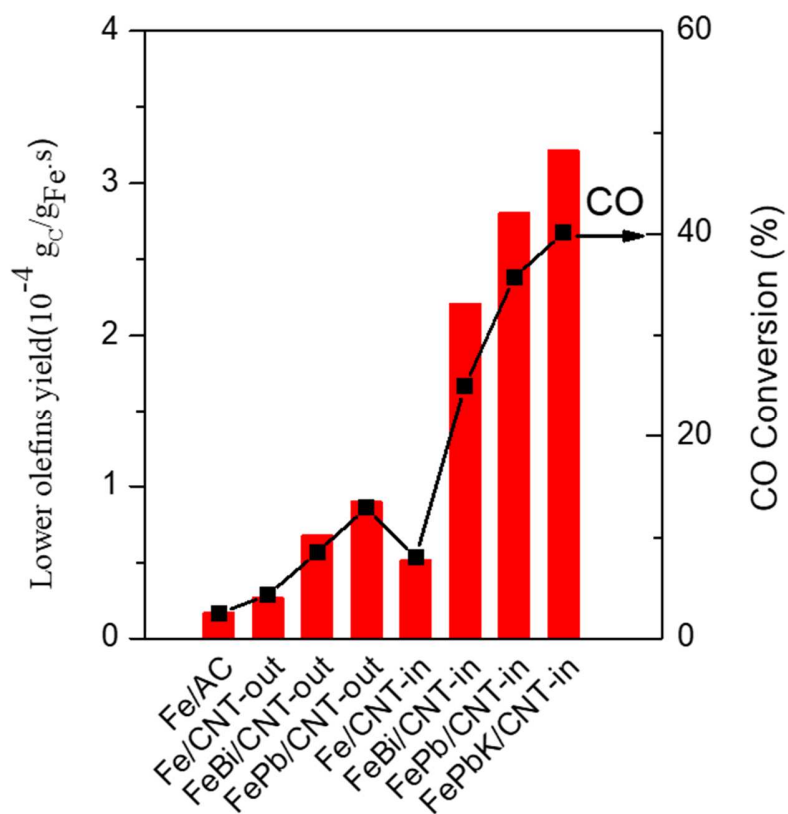
**Figure 11.** Catalyst magnetization measured: (a) during cooling down after CO treatment at 350 °C, (b) during cooling down after syngas treatment at 350 °C.



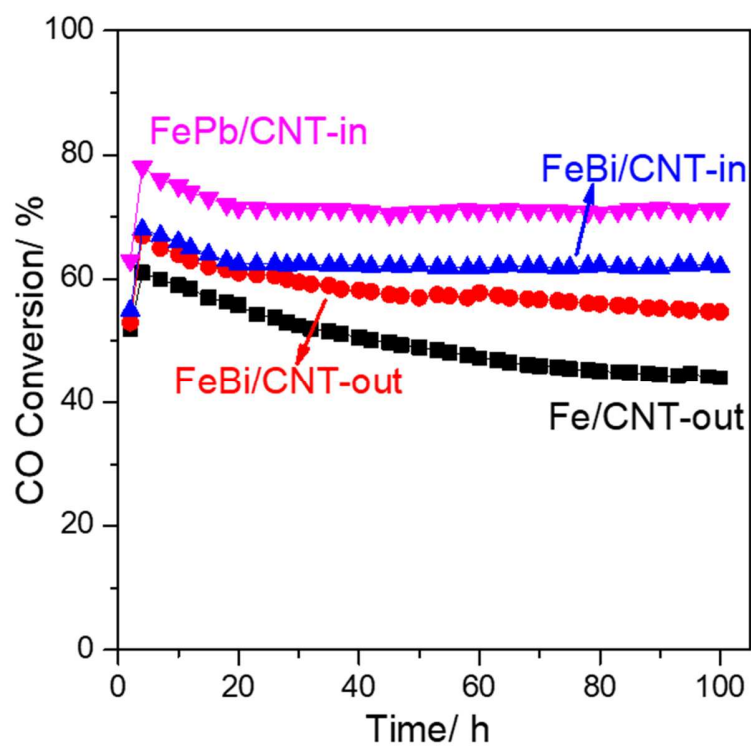
**Figure 12.** Product selectivity versus CO conversion over CNT confined and non-confined iron catalysts. Reaction conditions:  $W = 0.1$  g,  $H_2/CO = 1$ ,  $P = 10$  bar,  $T = 350$  °C,  $GHSV = 10.2-30.6$  L h<sup>-1</sup>g<sup>-1</sup>.



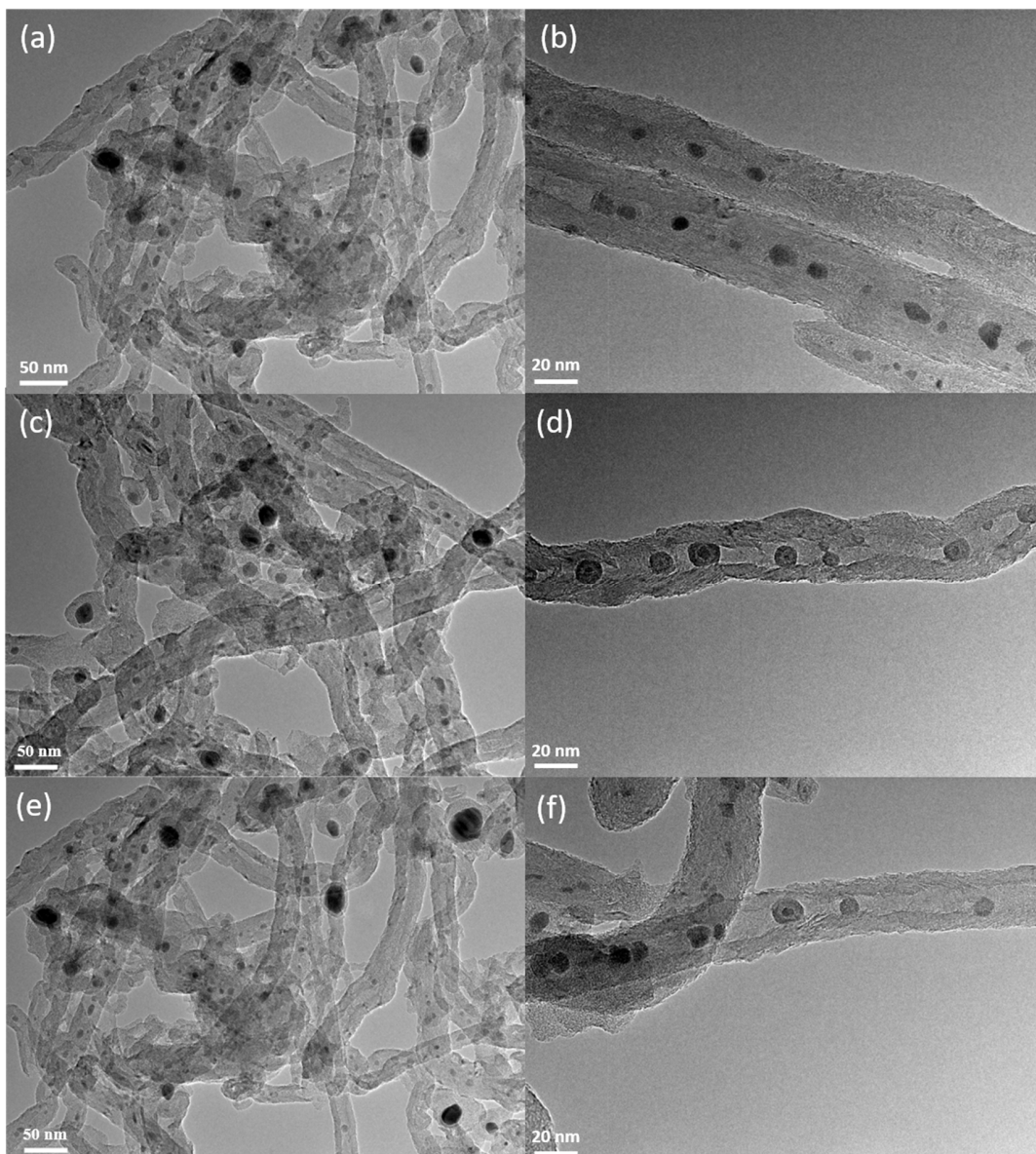
**Figure 13.** Simplified schema of FT reaction



**Figure 14.** Light olefins selectivity and CO conversion over the confined and non-confined iron-based catalysts. Reaction conditions:  $W = 0.1 \text{ g}$ ,  $\text{H}_2/\text{CO} = 1$ ,  $P = 1 \text{ bar}$ ,  $T = 350 \text{ }^\circ\text{C}$ ,  $GHSV = 3.4 \text{ L h}^{-1}\text{g}^{-1}$ .

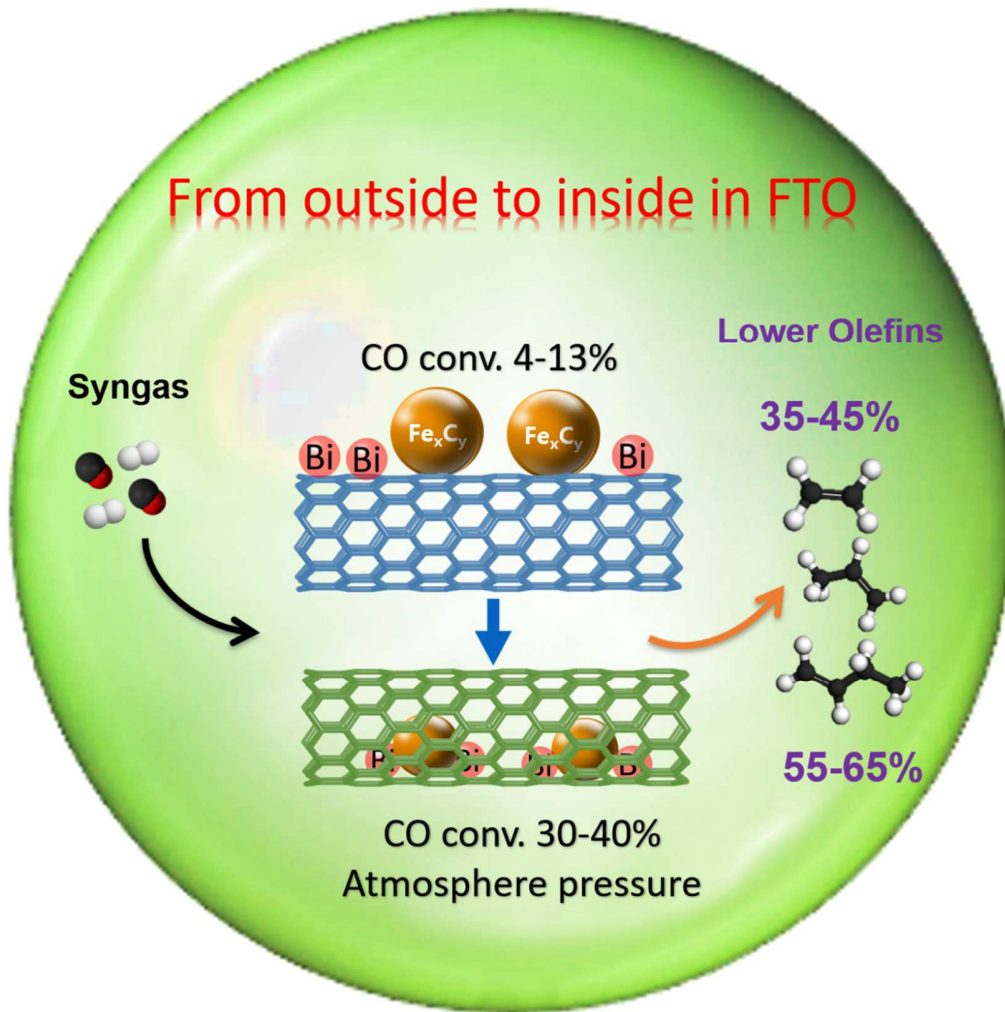


**Figure 15.** CO conversion as a function of time on stream for CNT confined and non-confined iron-based catalysts. Reaction conditions:  $W = 0.1$  g,  $H_2/CO = 1$ ,  $P = 10$  bar,  $T = 350$  °C,  $GHSV = 6.8-20.4$  L h<sup>-1</sup>g<sup>-1</sup>.



**Figure 16.** TEM micrographs for spent confined and non-confined Fe catalysts after reaction: (a) Fe/CNT-out-R, (b) Fe/CNT-in-R, (c) FeBi/CNT-out-R, (d) FeBi/CNT-in-R, (e) FePb/CNT-out-R, (e) FePb/CNT-in-R.

## From outside to inside in FTO



Graphic abstract for promotion and confinement effect in FTO